



Facultad de Ciencias

**Berezinskii– Kosterlitz–Thouless phase  
transitions in  $\text{PbTiO}_3/\text{SrTiO}_3$   
superlattices**

(Transiciones de fase de Berezinskii– Kosterlitz–Thouless en  
superredes de  $\text{PbTiO}_3/\text{SrTiO}_3$ )

Trabajo de Fin de Máster  
para acceder al título de

**MÁSTER INTERUNIVERSITARIO EN QUÍMICA  
TEÓRICA Y MODELIZACIÓN COMPUTACIONAL**

Autor: Fernando Gómez Ortiz

Director: Javier Junquera Quintana

03/07/2020



## Acknowledgements

En primer lugar, agradecer al departamento de Ciencias de la Tierra y Física de la Materia Condensada por el buen trato recibido siempre, no fue un comienzo de año sencillo en cuanto a lo burocrático, sin embargo, nunca faltó vuestro apoyo y ánimo. Este trabajo no habría sido posible en otras circunstancias, gracias.

En especial, a Pablo y cómo no, a Javier por vuestro tiempo, interés y duro trabajo es un placer poder hacer mi tesis junto a vosotros y contagiarme, no sólo de vuestros conocimientos, sino también de vuestra pasión por la física.

A mi familia, padres y hermano, que siempre esperan de mi lo máximo; gracias por el apoyo, cariño y preocupación por intentar comprender lo que hago, aunque muchas veces, no sea de fácil explicación. Siempre me habéis dejado dedicarme a lo que me gusta y así, sin quererlo, este trabajo también resulta ser vuestro. Acordarme como siempre también de mi abuelo que sé que estaría orgulloso.

A la gente que comparte mi vida, mis compañeros de física, Guridi, Leti, Andrea, Gus. Gracias por todo.

Por último, gracias a la beca FPU, que tanto costó disfrutar una vez conseguida, por el sustento económico. Espero que este trabajo marque el inicio de una bonita tesis y, con suerte, carrera académica. Prometo esforzarme...

*...alea iacta est*



## Abstract

In the present work we shall study the basic theory behind the celebrated Berezinskii–Kosterlitz–Thouless (BKT) topological phase transitions. In order to do so, we first introduce the simple XY-model, where these phase transitions were initially discovered. Within this context, we compute the energy of an isolated topological defect (a vortex) and the interaction energy between a collection of localized defects. Then, with the help of the correlation functions, we characterize the different orderings of the phases that appear as a function of temperature: from the quasi-long-range order at low temperatures to a fully disordered phase at high-temperature. This study sets the grounds for introducing the Berezinskii–Kosterlitz–Thouless (BKT) topological phase transitions. A bibliographic search is made to study how the different assumptions present in the XY-model (dimensionality of space, dimensionality of the order parameter, presence of long-range interactions and/or continuous symmetry in the Hamiltonian), affect the eventual existence of such phase transitions. Special attention is paid to the recent discovery of BKT transitions in ferroelectric systems. Finally, we carry out second-principles simulations in  $\text{PbTiO}_3/\text{SrTiO}_3$  superlattices and reveal the presence of topological phase transitions both when the polarization in the  $\text{PbTiO}_3$  layers is fully contained in the  $xy$ -plane, and where the polarization texture displays alternating clockwise/counter-clockwise vortices in the  $xz$ -plane.

**Keywords:** BKT, topological phase transitions, Mermin-Wagner theorem, correlation functions, vortices, ferroelectricity, second-principles simulations,  $\text{PbTiO}_3/\text{SrTiO}_3$  superlattices.

## Resumen

En este trabajo se ha estudiado la teoría básica detrás de las famosas transiciones de fase topológicas de Berezinskii–Kosterlitz–Thouless (BKT). Para ello, primero hemos introducido el modelo XY en el que estas transiciones fueron descubiertas por primera vez. En este contexto se calcula la energía de un defecto aislado (vórtice) así como la de una colección localizada de ellos. Seguidamente, con la ayuda de las funciones de correlación se ha caracterizado los diferentes ordenamientos de las fases que aparecen como función de la temperatura: desde el cuasi-largo alcance a bajas temperaturas hasta el desorden a altas. Este estudio fija las bases para introducir las transiciones de fase BKT. Se realizó una búsqueda bibliográfica para estudiar cómo las diferentes asunciones presentes en el modelo XY (dimensionalidad del espacio, del parámetro de orden, presencia de interacciones a largo alcance y simetrías continuas del Hamiltoniano), afectan a la posible existencia de dichas transiciones. Se presta especial atención a recientes descubrimientos de la presencia de transiciones BKT en sistemas ferroeléctricos. Finalmente, se realizaron simulaciones desde segundos principios en superredes de  $\text{PbTiO}_3/\text{SrTiO}_3$  que revelan la existencia de transiciones de fase topológicas tanto cuando la polarización del  $\text{PbTiO}_3$  está confinada en el plano  $xy$  como cuando el patrón de polarización presenta una estructura formada por vórtices horarios y antihorarios en el plano  $xz$ .

**Palabras clave:** BKT, transición de fase topológicas, teorema de Mermin-Wagner, función de correlación, vórtices, ferroelectricidad, simulaciones desde segundos-principios, superredes  $\text{PbTiO}_3/\text{SrTiO}_3$



# Contents

<b>1</b>	<b>Introduction</b>	<b>1</b>
<b>2</b>	<b>The two dimensional XY-model</b>	<b>2</b>
<b>3</b>	<b>Local minima of the Hamiltonian: Vortex textures</b>	<b>4</b>
3.1	T = 0 K case . . . . .	4
3.2	Finite temperature case . . . . .	5
<b>4</b>	<b>Interaction energy between singularities</b>	<b>10</b>
<b>5</b>	<b>Mermin-Wagner Theorem, ground state solutions.</b>	<b>15</b>
5.1	Correlation function. Definition and particular cases. . . . .	15
5.2	Correlation function in the low Temperature regime . . . . .	19
5.3	Correlation function in the high Temperature regime . . . . .	21
<b>6</b>	<b>Berezinskii-Kosterlitz-Thouless transition</b>	<b>26</b>
6.1	Topological phase transition . . . . .	27
<b>7</b>	<b>Critical analysis of the XY-model</b>	<b>30</b>
7.1	Influence of the short-range interactions . . . . .	30
7.2	Influence of the continuous symmetry . . . . .	30
7.3	Influence of the dimensionality of the order parameter . . . . .	31
7.3.1	One dimensional order parameter . . . . .	32
7.3.2	Two dimensional order parameter . . . . .	32
7.3.3	Three dimensional order parameter . . . . .	33
7.4	Influence of the dimensionality of the system . . . . .	35
<b>8</b>	<b>Topological phase transitions in <math>\text{PbTiO}_3/\text{SrTiO}_3</math> superlattices.</b>	<b>39</b>
8.1	First Model: polarization lying in the $xy$ plane. . . . .	40
8.2	Second Model: vortex textures in the polarization pattern . . . . .	45
<b>9</b>	<b>Conclusions</b>	<b>57</b>
<b>A</b>	<b>Energy of different spin textures.</b>	<b>61</b>
<b>B</b>	<b>Resolution of singularities via renormalization.</b>	<b>63</b>
<b>C</b>	<b>Derivation of the energy of interacting singularities</b>	<b>65</b>
<b>D</b>	<b>Computational aspects.</b>	<b>67</b>



# 1 Introduction

In many occasions, the physics of two dimensional systems differ from the properties of bulk materials, resulting in surprising effects that are counterintuitive for our common experience in three dimensions. One of those examples can be found in the presence or absence of phase transitions as a function of temperature.

A paradigmatic example is the case of ferromagnets, that can be described by a simple model: the Heisenberg Hamiltonian,  $\mathcal{H} = -J \sum_{\langle ij \rangle} \mathbf{S}_i \cdot \mathbf{S}_j$ , where  $\mathbf{S}_i$  is the spin at a particular site  $i$  of a lattice, that can point in any direction, and interacts only with first-neighbours  $\langle ij \rangle$ . In three-dimensions, and assuming  $J > 0$ , the ground state at zero-temperature is a ferromagnetic state where all the spins are ordered, pointing in the same directions. In the absence of an external magnetic field, the direction for the alignment is arbitrary, not defined; the ground state is degenerate for whatever direction of the spins. Independently of the range of the interaction, at low enough temperature an ordered phase with a non-vanishing average magnetization can be defined. If the temperature is farther increased, thermal energy destabilizes the system and a classical ferromagnetic to paramagnetic second order phase transition occurs.

The situation is different in two-dimensions. In a pioneering work by Mermin and Wagner in 1966 (1), it was proved how in a two-dimensional slab of spins that can point anywhere in the plane, and that interact with their first neighbours through short range interactions presenting a continuous symmetry (the so-called XY-model), no ordered state is possible at any finite temperature, in contrast with the previous experience in three-dimensions. Therefore, this result made impossible the existence of a usual temperature-driven order-disorder phase transition, and for many years it was thought that phase transitions were elusive as a function of temperature for such kind of systems. It was not until the early seventies of the last century when the groundbreaking works of Kosterlitz and Thouless (2; 3) showed how indeed a phase transition at finite temperature is possible. But the nature of the phase transitions is different from the usual ones: now topological excitations called vortices played an essential role (4). These vortices are topological defects that cannot be transformed into the monodomain ground state, where all the spins are aligned, by a continuous rotations of the spins. Similar phase transitions were discussed one year before the milestone publication of Kosterlitz and Thouless by the russian physicist Vadim Berezinskii (5; 6) (died in 1980). These transitions were coined after them as Berezinskii-Kosterlitz-Thouless (BKT) topological phase transitions.

Nowadays, BKT phase transitions are present in many fields. For instance, they have been invoked to explain phase transitions in Josephson junction arrays(7; 8), thin disordered superconducting granular films and the superconductor to insulator transition(9; 10), or dislocations in two-dimensional materials(3). Even beyond condensed-matter physics, they are applied in atomic physics or statistical mechanics. Due to the universality and the importance of these phase transitions, Kosterlitz and Thouless were

awarded with the Noble prize in Physics in 2016 for “theoretical discoveries of topological phase transitions and topological phases of matter”.

In this work, we shall focus on the study of the XY-model, one of the simplest model where these phase transitions appear. We shall give explicit equations for the energy of a vortex structure, and of a pair of topological defects. From these derivations, we shall explain the absence of an ordered phase at finite temperatures, together with the mechanism for the topological phase transition. After the study of such a simple model, we shall make a critical analysis about how the different assumptions in the model (dimensionality of the system, dimensionality of the order parameter, influence of the long-range interactions, etc.) affect the eventual existence of the phase transitions. Finally, we shall investigate how these phase transitions can be found in ferroelectric/dielectric superlattices, even if these systems do not accomplish some of the restrictions of the XY-model.

## 2 The two dimensional XY-model

Our reference model through this work will be the two dimensional XY-model which is constituted by planar rotors of unit length arranged on a two dimensional square lattice. The rotors can point in any direction contained on the plane of the layer, generalizing what happens in the Ising model where the rotors can only point in two opposite directions. A given rotor  $i$  will be characterized by only one parameter: the angle  $\theta_i$  that it forms with respect to the horizontal axis as it is depicted in Fig. 2.  $\theta_i$  can take any value between 0 and  $2\pi$ .



Figure 1: Parametrization of a given rotor in the space by the angle it forms with the horizontal line. The arrow, that represents the local spin at a given point in space, has one unit length.

The Hamiltonian of the system under these constrains can be written as

$$\mathcal{H} = -J \sum_{\langle i,j \rangle} \mathbf{S}_i \cdot \mathbf{S}_j, \quad (1)$$

where we have assumed that a given rotor interacts only with its first neighbours, represented by  $\langle i, j \rangle$  in the sum. Within this notation we shall assume that each interaction between a pair of spins is counted only once. The Hamiltonian in Eq. (1) can be simplified if we write  $\mathbf{S}_i$  as a function of the order parameter  $\theta_i$  as  $\mathbf{S}_i = (\cos \theta_i, \sin \theta_i)$ , so

$$\begin{aligned}
\mathcal{H} &= -J \sum_{\langle i, j \rangle} \mathbf{S}_i \cdot \mathbf{S}_j \\
&= -J \sum_{\langle i, j \rangle} (\cos \theta_i \cos \theta_j + \sin \theta_i \sin \theta_j) \\
&= -J \sum_{\langle i, j \rangle} \cos(\theta_i - \theta_j),
\end{aligned} \tag{2}$$

where we have used the trigonometric relation  $\cos a \cos b + \sin a \sin b = \cos(a - b)$ .

If we now assume that the rotors varies smoothly from site to site, so  $\theta_i - \theta_j$  is small, then we can approximate  $\cos x \approx 1 - \frac{x^2}{2}$  in Eq. (2). This approximation is sensible at low enough temperatures, due to the fact that we are considering first neighbour sites. However, at high temperatures we will no longer be able to assume this simplification. Therefore,

$$\begin{aligned}
\mathcal{H} &= -J \sum_{\langle i, j \rangle} \cos(\theta_i - \theta_j) \\
&\approx -J \sum_{\langle i, j \rangle} \left[ 1 - \frac{1}{2} (\theta_i - \theta_j)^2 \right] \\
&= -2NJ + \frac{J}{4} \sum_i [(\theta(x_i, y_i) - \theta(x_{i+1}, y_i))^2 + (\theta(x_i, y_i) - \theta(x_{i-1}, y_i))^2 + \\
&\quad + (\theta(x_i, y_i) - \theta(x_i, y_{i+1}))^2 + (\theta(x_i, y_i) - \theta(x_i, y_{i-1}))^2],
\end{aligned} \tag{3}$$

where  $N$  represents the total number of rotors of the system. To compute the terms in the right-hand-side of Eq. (3) we have consider a factor  $1/2$  to avoid the double counting of the energy of one spin with its four first-neighbours. Finally we shall take the continuum limit of the lattice in Eq. (3), assuming that the size of the system is much larger than the spacing between first neighbours, so we have

$$\begin{aligned}
\theta(x_i, y_i) - \theta(x_{i+1}, y_i) &\approx \theta(x_i, y_i) - \left( \theta(x_i, y_i) + a \frac{\partial \theta}{\partial x} \Big|_{(x_i, y_i)} \right) \\
&= -a \frac{\partial \theta}{\partial x} \Big|_{(x_i, y_i)},
\end{aligned} \tag{4}$$

and a similar expression along the  $y$ -direction. Replacing Eq. (4) into Eq. (3)

$$\begin{aligned}\mathcal{H} &= -2NJ + \frac{J}{4} \sum_i 2a^2 \left[ \left( \frac{\partial\theta}{\partial x} \right) \Big|_{(x_i, y_i)}^2 + \left( \frac{\partial\theta}{\partial y} \right) \Big|_{(x_i, y_i)}^2 \right] \\ &= -2NJ + \frac{J}{4} \sum_i 2a^2 |\nabla\theta_i|^2,\end{aligned}\tag{5}$$

and taking the limit when  $a \rightarrow 0$  in Eq. (5), we can write the Hamiltonian of the problem in its continuum form being consistent with the basic bibliography, such as Eq. (43) of one of the original papers by Kosterlitz and Thouless, Ref. (3).

$$\mathcal{H} \approx -2NJ + \frac{J}{2} \int \int dxdy (\nabla\theta(x, y))^2.\tag{6}$$

Notice that the Hamiltonian in Eq. (6) is symmetric under the rotations of all the spins around an axis perpendicular to the plane, represented by the orthogonal matrices ( $2 \times 2$ ), i. e. the  $\mathcal{O}(2)$  symmetry group. This will be an important issue that we shall refer in the following Sections.

### 3 Local minima of the Hamiltonian: Vortex textures

#### 3.1 $T = 0$ K case

At  $T = 0$  K the configuration that minimizes the energy is an ordered phase where all spins are parallel to each other. In such situation, the integral in the right-hand-side of Eq. (6) vanishes and the ground state energy equals  $-2NJ$ . This configuration is infinitely degenerated: if all the spins are aligned with the same angle  $\theta_i$  the energy is at the minimum and has the same value, independently of the angle. Notice that all these infinite collection of degenerated configurations can be distinguished by the direction of the overall magnetization  $\mathbf{M} = \sum_i \frac{\mathbf{S}_i}{N}$ , as it is shown in Fig. 2.

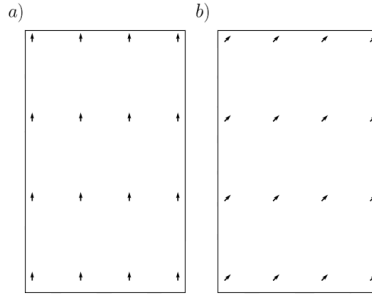


Figure 2: Two different degenerated states related by a rotation of  $\frac{\pi}{4}$ .

The states in Fig. 2(a) and Fig. 2(b) are clearly different: the order parameter, i.e. the magnetization, points along different directions, but they are exactly degenerated in energy. If we apply one of the symmetry operations of the Hamiltonian to the state of Fig. 2(a), that means if we rotate all the dipoles by the same amount, then we end up in a state that can be distinguished from the original one [for instance, the one represented in Fig. 2(b) for a rotation angle of  $\theta_i = 45^\circ$ ]. Therefore, we have broken the continuum symmetry of the Hamiltonian; if the symmetry would be preserved, we should end up in another state indistinguishable from the original one.

As we shall see in Section 5 below, and as a consequence of the Mermin-Wagner theorem -which states that a two-dimensional system with short range interactions presenting a continuous symmetry cannot spontaneously break this symmetry at any finite temperature- these solutions are not possible for any non-zero temperature. Therefore, our system tends to adopt different configurations. In the next Section we shall explore which arrangements minimize the Hamiltonian.

### 3.2 Finite temperature case

At finite temperature, where thermal fluctuations favours the canting of neighbour spins, new configurations that corresponds to local minimum of the Hamiltonian are accessible. Moreover, as we have mentioned we know that constant solutions are not physically possible so we would be interested in finding different types of minima. The fields that corresponds to local minima of  $\mathcal{H}$  are solutions to  $\frac{\delta \mathcal{H}}{\delta \theta} = 0$ , where we have to take the functional derivative of  $\mathcal{H}$  with respect to  $\theta$ . To perform this functional derivative, and for the sake of brevity in the notation, we shall replace the coordinates where a rotor is located  $(x, y)$  by  $\mathbf{r}$ . Then, we perturb the rotation pattern  $\theta(\mathbf{r}')$  going point by point in space and adding an infinitesimal extra rotation  $\epsilon$  to the particular rotor located at point  $\mathbf{r}$ , and compute how the energy changes [see Chapter 6.1 of Ref. (11)].

$$\frac{\delta\mathcal{H}}{\delta\theta(\mathbf{r})} = \lim_{\epsilon \rightarrow 0} \frac{1}{\epsilon} \iint d\mathbf{r}' [\nabla(\theta(\mathbf{r}') + \epsilon\delta(\mathbf{r}' - \mathbf{r}))]^2 - \iint d\mathbf{r}' (\nabla\theta(\mathbf{r}'))^2.$$

Knowing that  $\nabla$  operator is linear, expanding the square and ignoring terms which depends on  $\epsilon^2$  that disappear when taking the limit, we arrive to

$$\begin{aligned} \frac{\delta\mathcal{H}}{\delta\theta(\mathbf{r})} &= \lim_{\epsilon \rightarrow 0} \frac{1}{\epsilon} \iint d\mathbf{r}' \left( \cancel{(\nabla\theta(\mathbf{r}'))^2} + 2\epsilon\nabla\theta(\mathbf{r}')\nabla\delta(\mathbf{r}' - \mathbf{r}) + \cancel{\epsilon^2(\nabla\delta(\mathbf{r}' - \mathbf{r}))^2} \right) \mathcal{O}(2) \\ &\quad - \iint d\mathbf{r}' \cancel{(\nabla\theta(\mathbf{r}'))^2} \\ &= \lim_{\epsilon \rightarrow 0} \frac{2}{\epsilon} \iint d\mathbf{r}' \epsilon\nabla\theta(\mathbf{r}')\nabla\delta(\mathbf{r}' - \mathbf{r}) \\ &= -2\nabla^2\theta, \end{aligned}$$

where, in the last step, we have used the properties of integration of the derivative of a delta function [in particular  $\int f(x)\delta'(x)dx = -\int f'(x)\delta(x)dx$ ].

Finally, to find stationary solutions of the Hamiltonian, what we have to solve is a two dimensional Laplace equation of the form

$$\nabla^2\theta = 0. \tag{7}$$

There are different types of solutions for Eq. (7). First, the trivial solution where  $\theta(x, y)$  is constant corresponds to the ground state ( $T = 0$  K), since the second term in Eq. (6) vanishes. But, besides that homogeneous case, there might be other non-trivial solutions where the order parameter adopts a *vortex* type topology that also minimize the Hamiltonian and are physically possible at finite temperatures.

To find this new family of solutions, we should first define the boundary conditions determined by the fact that the angle  $\theta$  should return to itself if a excursion around a closed circle in the  $(x, y)$  plane is made. The change of the order parameter after taking an infinitesimal length of this excursion is given by  $d\theta = \nabla\theta(x, y) \cdot d\mathbf{l}$ , so the boundary condition translates into the fact that the circulation of the field  $\theta$  along a closed loop is

$$\oint \nabla\theta(x, y) \cdot d\mathbf{l} = 2\pi n, \tag{8}$$

where  $n \in \mathbb{Z}$ , since the vector in the start and the end of the loop must point in the same direction.

When  $n = 0$  we have no singularities in the vector field. That means that the field lines (i.e integral curves) are well defined for every point in space and the solution is topologically equivalent to the constant solution studied before. By topologically equivalent we mean that we can continuously transform one to another without the creation or annihilation of any defect (i.e without forcing any vector to vanish).

However, in order to have a solution with  $n \neq 0$  in Eq. (8), the circuit along which we take the circulation must enclose what we call a singularity of the vector field. In this context a singularity is a point  $\mathbf{r}$  where our vector field vanishes. More rigorously, the reason why we call them singularities can be understood if we think on the vector field as “velocity curves”. Due to the Cauchy theorem of uniqueness and existence of solution in differential equations, given a direction (a vector) and a point we only have one integral curve passing through it. However, when the vector field vanishes at a given point, we do not have any information about the integral curves at that point: they are ill-defined there. Through that point it might pass zero (a clock-wise vortex), one (a dipole) or infinite (a source) integral curves. Mathematically these points are singular in the sense that they are rare, we need to study its neighbourhood in order to understand them.

Physically those points are interesting because singularities will correspond to defects of our material. In this work we shall focus on point-like defects. However, higher dimensional defects are also recurrent in condensed matter and can be studied with techniques similar to the ones developed in this work.

We shall define index of the singularity  $I(\mathbf{v}, \mathbf{r})$  or equivalently, vorticity  $n$  of the vector field  $\mathbf{v}$  at the point  $\mathbf{r}$  as the number of times that the vector field wraps the unit sphere  $\mathbb{S}^1$  of radius  $\epsilon$  centred in  $\mathbf{r}$ . The degree of the vector field will be the sum of the indexes of all its singularities  $deg(\mathbf{v}) = \sum_{\mathbf{r} \in Sing} I(\mathbf{v}, \mathbf{r})$  and can be thought to be the global vorticity of the vector field. We can see a sketch of how to compute this index in Fig. (3). The vorticity is independent of the radius as long as  $\mathbf{r}$  is the only singularity enclosed by the circumference.

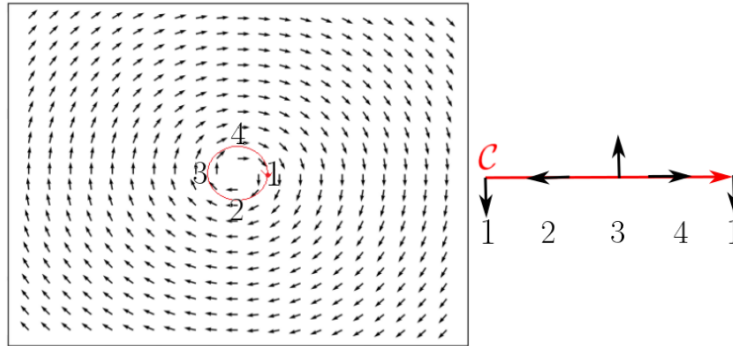


Figure 3: Vortex with vorticity equal to 1. We can see how, when following the red closed path in the left panel in the counter-clock-wise sense, the vector field performs one complete turn in the same sense of direction (right panel). Since the sense of rotation in the circulation is the same as the sense of rotation of the vector field, the vorticity is taken as positive. If the sense would be the opposite, then the sign of the vorticity would be taken as negative, as is the case of antivortices.

One particular example of a vector field with a singularity is given by the well-known field

$$\theta = \arctan\left(\frac{y}{x}\right), \quad (9)$$

which presents a singularity in  $(0,0)$  and is easy to prove that fulfills Eq. (7) at every point in the two-dimensional space since,

$$\nabla^2\theta = \frac{2yx}{(x^2 + y^2)^2} + \frac{-2yx}{(x^2 + y^2)^2} = 0,$$

and has the form presented in Fig. 4

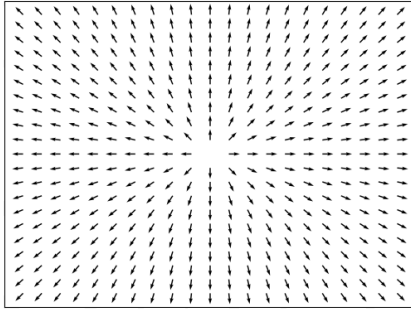


Figure 4: Example of one non trivial solution for Eq. (7), where the angle of a rotor located at  $\mathbf{r} = (x, y)$  is defined after Eq. (9) as  $\theta = \arctan\left(\frac{y}{x}\right)$  this type of vortex is usually denoted as a “source” since from the singularity infinitely many integral curves are born.

Taking advantage of the fact that we know the analytical expression of the vector field, we can compute the energy of this vortex solution. Taking the origin of the energies at the energy level of the perfectly order solution  $[-2NJ$  in Eq. (6)], then we have to compute only

$$E = \frac{J}{2} \iint dxdy |\nabla\theta(x, y)|^2 = \frac{J}{2} \iint dxdy \frac{x^2 + y^2}{(x^2 + y^2)^2}, \quad (10)$$

that changing to polar coordinates is easily solved

$$\begin{aligned}
E &= \frac{J}{2} \iint dxdy \frac{x^2 + y^2}{(x^2 + y^2)^2} \\
&= \frac{J}{2} \iint r dr d\theta \frac{r^2}{r^4} \\
&= \frac{J}{2} \int_a^L dr \frac{2\pi}{r} \\
&= 2\pi \frac{J}{2} \ln(r) \Big|_a^L \\
&= \pi J \ln \left( \frac{L}{a} \right). \tag{11}
\end{aligned}$$

In Eq. (11) the integration limits are determined by the system size  $L$  (upper limit) and by the discrete nature of our problem, where the rotors are separated by a distance  $a$ <sup>1</sup>(lower limit).

The previous expression for the energy has been obtained for the particular vector field described in Eq. (9). However, as we explain in Appendix A this is, in fact, a general result and the energy of an isolated vortex can be expressed in terms of its vorticity  $n$  as

$$E_{\text{vor}} = \pi n^2 J \ln \left( \frac{L}{a} \right), \tag{12}$$

in agreement with Eq. (44) of the original paper of Kosteritz and Thouless, Ref. (3)

Just as an exercise and to keep in mind the dependence with the system size we plot Eq. (12) for the case  $a = 1$ ,  $J = \frac{1}{\pi}$ ,  $n = 1$ . In the thermodynamic limit this energy obviously diverges.

---

<sup>1</sup>The closer we are to the singularity, the faster the spin texture varies, here we are assuming that even at a distance of one unit cell (i.e.  $a$ ) near the singularity  $\theta_i - \theta_j \approx \frac{\partial\theta}{\partial l}$  still holds. If not we should replace  $a$  by a given cutoff  $r_0$  and add a finite term related with what is called *Core Energy*. This term justify the physical intuition that topologically equivalent configurations like a source field (Fig. 4) or a clockwise vortex (Fig. 3) may have different physical energies.

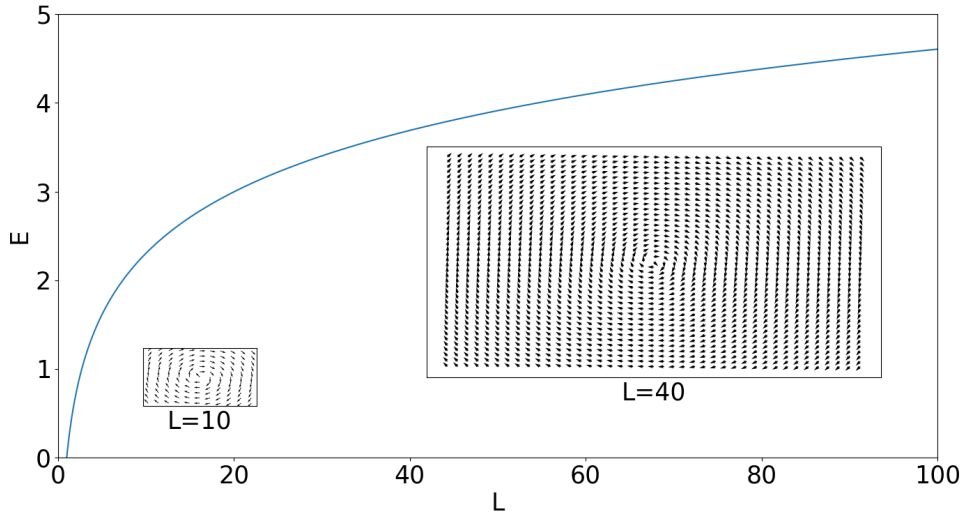


Figure 5: Energy dependence of a vortex texture with the system size for the case  $a = 1$ ,  $J = \frac{1}{\pi}$ ,  $n = 1$ .

## 4 Interaction energy between singularities

In the former Section, we have computed the energy of an isolated vortex within the framework of the XY-model. Now we shall take an step further and compute the energy of a system made of an arbitrary number of topological defects. In Fig. 6 we represent the particularly important cases of an antivortex-vortex [Fig. 6(a)], and a vortex-vortex [Fig. 6(b)] configuration.

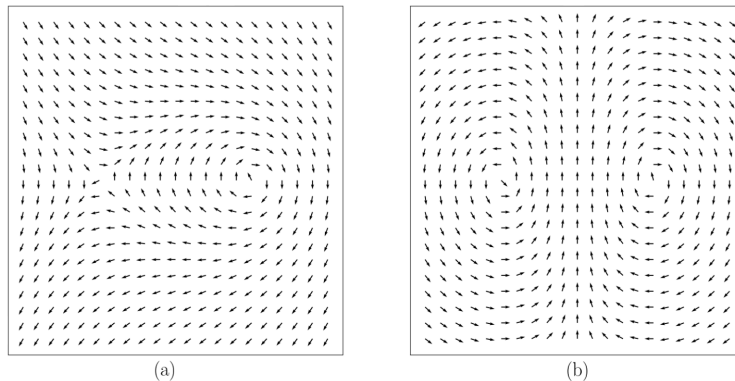


Figure 6: Spin texture of (a) an antivortex/clock-wise vortex configuration, and (b) a counter-clock-wise/clock-wise vortex pair. Since the vorticity for both the individual clockwise and counter-clock-wise vortices is equal to 1, and the vorticity for an isolated antivortex is equal to -1, the total vorticity of the system amounts to  $n = 0$  [panel (a)], and  $n = 2$  [panel (b)].

The starting point is the boundary condition of our problem, represented in Eq. (8), that can be rewritten in a way that help us to relate the vorticity number and the spatial location where the topological charge is generated. Indeed, according to the Stokes theorem, we can relate the circulation of the vector  $\nabla\theta$  along a closed loop with the flux of its curl over the surface enclosed by the loop,

$$\begin{aligned} \oint \nabla\theta \cdot d\mathbf{l} &= \iint \hat{e}_z \cdot (\nabla \times \nabla\theta) \, dxdy \\ &= \iint (\nabla \times \nabla\theta)_z \, dxdy = 2\pi n, \end{aligned} \quad (13)$$

where  $\hat{e}_z$  is a unitary vector perpendicular to the plane that contains the rotors, taken as the  $(x, y)$  plane.

If the surface enclosed by the path along which we compute the circulation does not include any singularity, then  $\nabla\theta$  can be written as the divergence of a derivable function  $\nabla\theta_0$  in all the points of the enclosed surface. Therefore, it fulfils the relation  $\nabla \times \nabla\theta_0 = 0$  (the rotational of a gradient always vanishes). Since  $n = 0$  (no topological defects), Eq. (13) holds.

However Eq. (13) shows that when we enclose a set of topological charges of charge  $n_i$  located at positions  $\mathbf{r}_i$ , our field is no longer derivable at those positions and, as proven in Appendix B, the curl of the gradient in these non-trivial cases amounts to

$$\nabla \times \nabla\theta = 2\pi \hat{e}_z \sum_i n_i \delta^2(\mathbf{r} - \mathbf{r}_i), \quad (14)$$

where it is implicit that  $\sum_i n_i = n$ , i.e. the total vorticity of the system. Moreover, in Appendix B it is also proved how this field can be expressed as a sum of a non-singular part ( $\theta_0$ ) and a topological part ( $\psi$ ) in such a way that

$$\nabla\theta = \nabla\theta_0 - \nabla \times \hat{e}_z\psi. \quad (15)$$

Our goal is to compute the energy for such a group of topological charges. In order to do so, we have to compute the integral of Eq. (6), that accounts for the deviation of the energy of the singularities with respect the ferromagnetic case,

$$\mathcal{H} = \frac{J}{2} \iint dx dy |\nabla\theta(x, y)|^2, \quad (16)$$

using the formal form of Eq. (15). As it is fully developed in Appendix C, the energy of such a collection of singularities is given by

$$E = \frac{J}{2}\pi C \sum_i n_i^2 - J \sum_i \sum_{i \neq j} \pi n_i n_j \ln(|\mathbf{r}_i - \mathbf{r}_j|), \quad (17)$$

The first term of Eq. (17) is related with the self-energy ( $C$  is the self-interaction constant), and the second term with the proper interaction between different vortices.

Several conclusions can be drawn from Eq. (17). For the sake of simplicity, in the following we shall assume the presence of only two singularities in our system. We shall focus on two different aspects, that can be summarized as:

(i) Evolution of the energy for singularities of the same or opposite vorticity. Figure 7 shows the dependency of the energy of the pair as a function of the distance between the cores of the singularities ( $r = |\mathbf{r}_i - \mathbf{r}_j|$ ) for singularities of the same (vortex/vortex or antivortex/antivortex) or opposite (vortex/antivortex) vorticities. We can see how the behaviour is similar to electrically charged particles: if the singularities present the same vorticity they repel each other (the minimum energy is obtained for a distance  $r \rightarrow \infty$ ), whereas if they present opposite vorticity they attract each other (the minimum energy is located at  $r \rightarrow 0$ ).

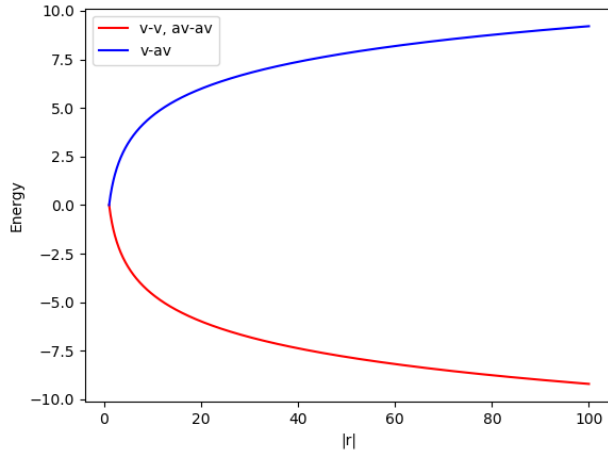


Figure 7: Interaction energy between two singularities depending on the distance between their cores ( $r = |\mathbf{r}_i - \mathbf{r}_j|$ ), and their respective vorticity. The red line represents the case where the two singularities do have the same vorticity [vortex/vortex (v-v) or antivortex/antivortex (av-av)], while the blue line represents the case where the two singularities have opposite vorticity [vortex-antivortex (v-av) pair]. We have assumed  $J = \frac{1}{\pi}$  and  $n_{i,j} = \pm 1$ . The zero of energies is taken at the self-energy given by the first constant term of Eq. (17).

(ii) The absence of a dependency on the system size  $L$  in the energy expression given by Eq. (17). To throw some light into this question and, in order to be as pedagogical as possible, we shall discuss this issue in a particular example instead of giving a rigorous proof. Let us assume that we have an antivortex/vortex pair as the one displayed in Fig. 8.

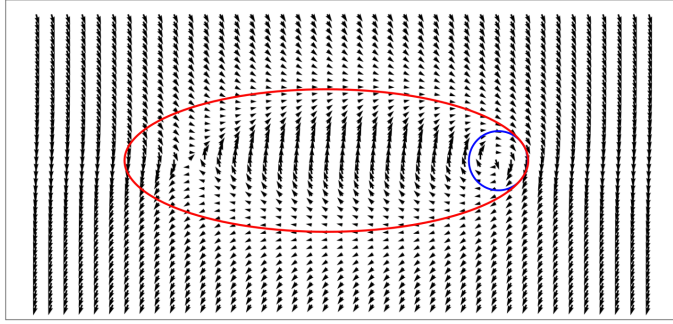


Figure 8: Antivortex-vortex spin texture with two circulation paths taken into account. The large red one encloses the two defects. The small blue circulation path encloses only the vortex.

If we compute the energy associated with the distortion of the field in the small circulation enclosed by the small blue circle, we would obtain only the effect of the encapsulated vortex. However, if we repeat the exercise and compute the energy associated with the texture enclosed by the larger red ellipse, that encompasses both the vortex and the antivortex, then the situation changes: the distortion produced by the vortex cancels out the distortions due to the antivortex in a sufficiently distant region and, therefore, the monodomain configuration is restored far away from the core of the singularities (see the dipoles at the rightmost and leftmost regions of Fig. 8). Since in Eq. (16) we are computing only the contribution of the energy due to the distortion with respect to the monodomain configuration, the cancellation of the distortions eliminates the dependence with the system size and leaves only the dependence with the distance between the defects: the closer they are the faster we get this cancellation of distortion and the less energetic our texture becomes. In fact, one can see that if we separate both to the limit of the system size we recover the previous result for isolated vortices.

Finally, after a careful study of Fig. 7, it is tempting to think that an spontaneous generation of many singularities maximally separated with same vorticity is energetically favoured. This would be true, but there are several constraints that we must consider before proposing this configuration. The first is that, as we mentioned in the derivation in Appendix C, only neutral configurations are energetically allowed. Therefore, we must keep the same number of vortex and anti-vortex in our system. The second is the finite size of our system, that prevents the arbitrary separation of the singularities when many of them are presented in the system. What happens in reality is that many vortex-antivortex pairs are generated so that if we have  $m$  vortices and  $m$  anti-vortices we have  $m^2$  attraction terms and  $m(m - 1)$  repulsion terms. The singularities change positions until an equilibrium is found. We would like to remark that this equilibrium is dynamic many vortex-antivortex pairs are annihilated and created during the process.

## 5 Mermin-Wagner Theorem, ground state solutions.

In this Section we shall try to give some insight on this famous theorem (1; 5). Although this is a very general result, we shall focus on the implications it has in the XY-model described in Sec. 2.

The Mermin-Wagner theorem states that a system with continuous symmetry and short-range interactions at finite temperature cannot be ordered i.e. cannot spontaneously break that symmetry.

Returning to Eq. (2) we can check that we are under the assumptions of the theorem:

- The Hamiltonian that describes the XY-model is short-range, since it only keeps first-neighbor interactions.
- The Hamiltonian is symmetric under any transformation ( $\theta \rightsquigarrow \theta + \phi$ ), i.e. if we rotate *all* the spins in the system by the same amount. Therefore, it presents a continuous  $\mathcal{O}(2)$  symmetry.

For  $T = 0$   $K$  the ground state would be a pure ferromagnetic state with all spins aligned in a well defined direction. Of course, it will be degenerate, since all the directions in the plane are equivalent. However, we shall see that this is not the case for any nearby infinitesimal temperature.

### 5.1 Correlation function. Definition and particular cases.

The figure of merit to detect the existence of phase transitions is the correlation function between spins,  $\langle \vec{S}_0 \cdot \vec{S}_{\mathbf{R}} \rangle$ , where  $\langle \dots \rangle$  represents the average of a certain quantity between all the accessible states at a given temperature. The evolution of the spin-spin correlation function with the temperature will determine the eventual existence of a topological phase transition.

In order to grasp the concept, let us first discuss the computation of the correlation function in a simplified system, schematized in the cartoon of Fig. 9 for a one-dimensional toy model representing sharp  $180^\circ$  domains periodically repeated in space. As it is shown in the cartoon we select the first spin in the supercell [marked with a red dot in Fig. 9(a)] and compute the average of the dot product of its spin with the first neighbours. Since the one at the right points in the same direction and the one at the left points in the opposite direction, the average of this dot product vanishes, as represented by the zero written on the right of the panel Fig. 9(a). Then, we proceed in the same way to compute the dot product of the spin taken as the origin with the second-, and subsequent neighbours, till all the possible pairs are considered. The procedure is repeated changing the spin considered as the origin, till all the spins in the supercell are covered, as shown by the change of the red dot in Fig. 9(b)-(f). Finally, for a given neighbour shell, the average is taken for all the spins, producing the profile shown in Fig. 9(g).

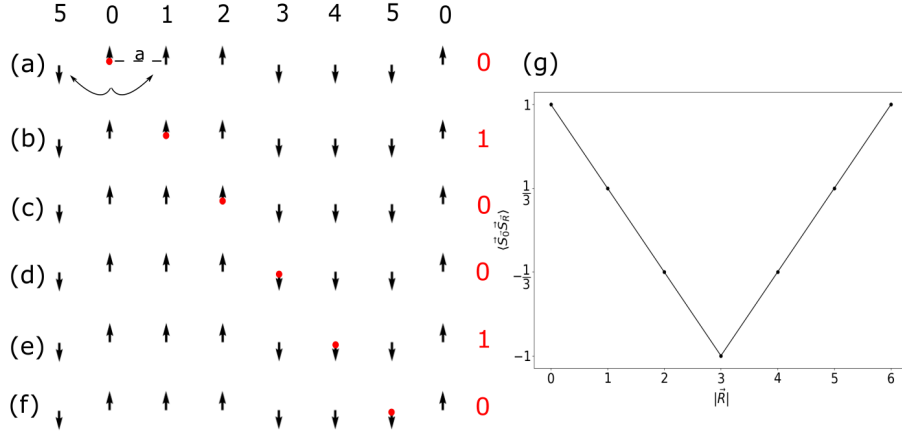


Figure 9: Schema followed to compute the correlation function. Panels (a)-(f) show the supercell of a one-dimensional toy model consisting in a periodic repetition of a unit cell that contains six spins, numbered from 0 to 5. The spins have been aligned to display perfect  $180^\circ$  domains. The spin taken as origin (red dot) changes from one panel to the other till all the spins in the unit cell are considered. The numbers at the right of the panels represent the average of the dot product of the spin at the origin with its first neighbours,  $\mathbf{R} = \pm a$ . To compute  $\langle \vec{S}_0 \cdot \vec{S}_{\mathbf{R}} \rangle$ , we average the results after considering all the possible spins as the origin. This overall average is taken in panel (g), when we can see how for the particular case of  $\mathbf{R} = \pm a$ ,  $\langle \vec{S}_0 \cdot \vec{S}_{\mathbf{R}=a} \rangle = 2/6$ . This procedure is repeated for all the neighbour shells, producing the black line in panel (g).

In the ferromagnetic ground state at  $T = 0$  K, this function will take constant value equal to 1, even at infinite distances. Indeed, the fingerprint of an ordered state of the system is to have a finite value of the correlation function at infinite distances. Three examples are shown in Fig. 10 for the monodomain configuration [Fig. 10(a)], where the correlation function is constant and equal to one; a periodically repeated  $180^\circ$  domain structure [Fig. 10(b)], with a correlation function following a sawtooth shape; and a cycloid spin structure [Fig. 10(c)], with a cosine type function for the correlation function.

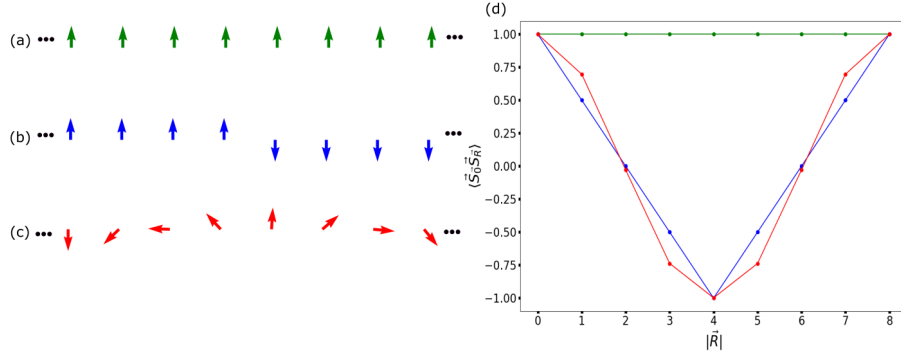


Figure 10: Correlation function  $\langle \vec{S}_0 \cdot \vec{S}_{\mathbf{R}} \rangle$  for three different ordered structures in a one-dimensional system: (a) a monodomain configuration (green), (b) a periodically repeated  $180^\circ$  domain structure (blue), and (c) a cycloid spin structure (red). The corresponding correlation function is shown in (d).

On the other hand the smoking gun to characterize a disordered state of the system is that the correlation function is arbitrarily small for sufficiently large distances. This localization of the correlation function might be strict, i.e. its value is strictly zero for  $|\mathbf{R}|$  larger than a given cutoff radius, or more gradual, with exponentially decaying values as a function of the distance.

But, is it possible an intermediate solution, where the correlation function does not take a finite value for infinite distances but its functional form decays slowly than the exponential? The answer is yes, and indeed that is the behaviour of the XY-model where, as we shall demonstrate below, the correlation function decays as a power law at low temperatures. Therefore, it does not strictly vanish at any given cutoff distance or presents an exponential decay (as in the disordered states). But it tends to zero when  $|\mathbf{R}| \rightarrow \infty$ , so we are not in the ordered case either. We shall refer to this type of ordering *quasi-long range order* (QLRO). This behaviour is strongly dependent of the temperature. Indeed, there is a critical value for which the correlation function starts to decrease exponentially. This change from a quasi-long range order to a disordered state is the hint of the presence of a phase transition.

In order to describe the transition in a more quantitative way, we define the spin-spin correlation function as

$$\begin{aligned}
 \langle \vec{S}_0 \cdot \vec{S}_{\mathbf{R}} \rangle &= \langle \cos(\theta_0 - \theta_{\mathbf{R}}) \rangle = \frac{1}{\mathcal{Z}} \int_{\text{accessible states}} \cos(\theta_0 - \theta_{\mathbf{R}}) e^{-\frac{\mathcal{H}_{\text{state}}}{k_B T}} \\
 &= \frac{1}{\mathcal{Z}} \int_0^{2\pi} \dots \int_0^{2\pi} \frac{d\theta_1 \dots d\theta_N}{(2\pi)^N} \cos(\theta_0 - \theta_{\mathbf{R}}) e^{-\beta \mathcal{H}_{\text{state}}}, \quad (18)
 \end{aligned}$$

where  $\beta = 1/k_{\text{B}}T$ ,  $k_{\text{B}}$  is the Boltzmann constant,  $T$  is the absolute temperature,  $\mathcal{H}_{\text{state}}$  is the energy of a particular spin configuration,  $N$  is the total number of spins in the system, and the integrals are taken so all the possible microstates of the system will be considered. In the language of the former simplified model presented before, we should:

- Sweep over all possible microstates of the system.
- For a particular microstate (let us take it as an instantaneous picture of the rotors), play the same game as before, summarized in Fig. 9, but now extended to a 2D system. Therefore, we have to consider one of rotors as the origin, compute the dot product with all the neighbours and tabulate its average as a function of the distance. Then, change the rotor consider as the origin and recompute the dot products and the averages as a function of the distance. The procedure is repeated till we have considered every rotor as the origin. Finally, compute the average of all the dot products as a function of the distance to the origin.
- Compute the energy of this microstate and weight the previous average with the Boltzmann factor.

In Eq. (18),  $\mathcal{Z}$  is the partition function of the system, defined as

$$\begin{aligned}
\mathcal{Z} &= \int_{\text{accessible states}} e^{-\frac{\mathcal{H}_{\text{state}}}{k_{\text{B}}T}} \\
&= \int_0^{2\pi} \dots \int_0^{2\pi} \frac{d\theta_1 \dots d\theta_N}{(2\pi)^N} e^{-\beta \mathcal{H}_{\text{state}}} \\
&= \int_0^{2\pi} \dots \int_0^{2\pi} \frac{d\theta_1 \dots d\theta_N}{(2\pi)^N} e^{-\beta (-J \sum_{\langle i,j \rangle} \cos(\theta_i - \theta_j))} \\
&= \int_0^{2\pi} \dots \int_0^{2\pi} \frac{d\theta_1 \dots d\theta_N}{(2\pi)^N} e^{\beta J (\sum_{\langle i,j \rangle} \cos(\theta_i - \theta_j))} \\
&= \int_0^{2\pi} \dots \int_0^{2\pi} \frac{d\theta_1 \dots d\theta_N}{(2\pi)^N} \prod_{\langle i,j \rangle} e^{\beta J \cos(\theta_i - \theta_j)} \\
&= \int \mathcal{D}[\theta] \prod_{\langle i,j \rangle} e^{\frac{J}{k_{\text{B}}T} \cos(\theta_i - \theta_j)}, \tag{19}
\end{aligned}$$

where we have made use of Eq. (2), and  $\int \mathcal{D}[\theta] = \int_0^{2\pi} \dots \int_0^{2\pi} \frac{d\theta_1 \dots d\theta_N}{(2\pi)^N}$  represents the integral over all the possible spin configurations divided by the total volume of the configurational space.

## 5.2 Correlation function in the low Temperature regime

In the low-temperature regime, we expect smooth variations in neighbouring spins orientations. Thus, for  $\beta J \gg 1 \Rightarrow (\theta_i - \theta_j) \ll 1$ . Then, we can profit of the derivation carried out in Sec. 2, where we observed: (i) how the cost of small fluctuations around the ground state can be obtained by a quadratic expansion, Eq. (3),

$$\begin{aligned} \mathcal{H} &= -J \sum_{\langle i,j \rangle} \cos(\theta_i - \theta_j) \\ &\approx -J \sum_{\langle i,j \rangle} \left[ 1 - \frac{1}{2} (\theta_i - \theta_j)^2 \right], \end{aligned}$$

in other words, the Hamiltonian is quadratic under small changes in the angles of the rotors; and (ii) how after performing a transition to the continuum limit the Hamiltonian can be written as summarized in Eq. (6),

$$\mathcal{H} \approx -2NJ + \frac{J}{2} \int \int dxdy (\nabla\theta(x, y))^2,$$

so the partition function takes the final form

$$\begin{aligned} \mathcal{Z} &= \int_{\text{accessible states}} e^{-\beta \mathcal{H}_{\text{state}}} \\ &= \int \mathcal{D}[\theta] e^{-\beta(-2NJ + \frac{J}{2} \int \int dxdy (\nabla\theta(x, y))^2)} \\ &= \int \mathcal{D}[\theta] e^{K(2N - \frac{1}{2} \int \int dxdy |\nabla\theta(x, y)|^2)} \\ &= \int \mathcal{D}[\theta] e^{2NK} e^{-\frac{K}{2} \int \int dxdy |\nabla\theta(x, y)|^2} \\ &= e^{2NK} \int \mathcal{D}[\theta] e^{-\frac{K}{2} \int \int dxdy |\nabla\theta(x, y)|^2}, \end{aligned} \tag{20}$$

where  $K = \beta J = \frac{J}{k_B T}$ , and the integral in the exponent is taken over all the spatial points in the plane. From now on, we shall omit the first exponential, that is just a simple constant. Since, as discussed above, the Hamiltonian is quadratic, the second exponential takes the functional form of a Gaussian.

Now that we have computed the partition function we are in good shape to obtain the correlation function, which gives the correlation between finding the rotor at  $\mathbf{R}$  at a certain angle when  $\theta_0$  is known. We only have to obtain the expected value of  $\vec{S}_0 \cdot \vec{S}_{\mathbf{R}}$ .

This can be done by integrating

$$\begin{aligned}\langle \vec{S}_0 \cdot \vec{S}_R \rangle &= \langle \cos(\theta_0 - \theta_R) \rangle = \mathcal{R} \langle e^{i(\theta_0 - \theta_R)} \rangle \\ &= \mathcal{R} \frac{\int \mathcal{D}[\theta] e^{i(\theta_0 - \theta_R)} \cdot e^{-K \int dx dy |\nabla \theta(x,y)|^2}}{\mathcal{Z}}\end{aligned}\quad (21)$$

Following ideas in Refs. (12; 13) and making profit of the mentioned Gaussianity of our distribution function in order to find the average of  $\langle \vec{S}_0 \cdot \vec{S}_R \rangle$  is not necessary to compute such an integral. According to the rules for Gaussian integration (14), we have the following relation to compute expected values of exponential functions like the one we are interested in ( $e^{i(\theta_0 - \theta_R)}$ )

$$\langle e^A \rangle = e^{\langle A \rangle + \frac{1}{2} \langle A^2 \rangle - \frac{1}{2} \langle A \rangle^2}.$$

Applying this rule to our case we have to substitute  $A \rightsquigarrow i(\theta_0 - \theta_R)$  and so

$$\begin{aligned}\langle A \rangle &\rightsquigarrow i \langle (\theta_0 - \theta_R) \rangle, \\ \langle A^2 \rangle &\rightsquigarrow - \langle (\theta_0 - \theta_R)^2 \rangle, \\ \langle A \rangle^2 &\rightsquigarrow - \langle (\theta_0 - \theta_R) \rangle^2.\end{aligned}$$

Therefore in order to obtain the correlation function we have to compute

$$\begin{aligned}\langle \vec{S}_0 \cdot \vec{S}_R \rangle &= \langle \cos(\theta_0 - \theta_R) \rangle = \mathcal{R} \langle e^{i(\theta_0 - \theta_R)} \rangle \\ &= \mathcal{R} e^{\langle i(\theta_0 - \theta_R) \rangle - \frac{1}{2} \langle (\theta_0 - \theta_R)^2 \rangle + \frac{1}{2} \langle (\theta_0 - \theta_R) \rangle^2}.\end{aligned}\quad (22)$$

Since we assume random thermal deviations from the reference angle  $\theta_0$ , and due to the parity of our Hamiltonian, then  $\langle (\theta_0 - \theta_R) \rangle = 0$ . This assumption can be done without any risk in this case because the shape of our Hamiltonian has to do with  $\cos(\theta_0 - \theta_R)$  and as the cosine function is even there is no energetic bias to cant spins in a certain direction which finally leads to a cancellation. However, in other systems this assumption might be false. Therefore

$$\langle \vec{S}_0 \cdot \vec{S}_R \rangle = \mathcal{R} e^{-\frac{1}{2} \langle (\theta_0 - \theta_R)^2 \rangle}.\quad (23)$$

Moreover, as it is proven in Ref. (12) that

$$\langle (\theta_0 - \theta_R)^2 \rangle = \frac{k_B T}{\pi J} \ln \left( \frac{|\mathbf{R}|}{a} \right).\quad (24)$$

Replacing Eq. (24) into Eq. (23), we obtain that the correlation function even for infinitesimally small temperatures is given by

$$\langle \vec{S}_0 \cdot \vec{S}_R \rangle = \left( \frac{a}{|\mathbf{R}|} \right)^{\frac{k_B T}{2\pi J}}.\quad (25)$$

This expression<sup>2</sup> shows how (i) the correlation function decays as a power factor of the distance between the spins, (ii) it goes to zero when the  $|\mathbf{R}| \rightarrow \infty$ , so the system is not in an ordered state (5; 6) as Mermin-Wagner theorem stated for such systems; and (iii) but this decay is not exponential, so the system is not in a fully disordered state. We are in one of the cases coined above where the system presents a quasi-long-range order. Only when  $T = 0$ , then the correlation function is equal to 1, independently of the distances between spins, and we are in the fully ordered ferromagnetic ground state. At any finite temperature however we move to this quasi-long-range ordered phase as predicted by the Mermin-Wagner theorem.

### 5.3 Correlation function in the high Temperature regime

In the high temperature regime we can no longer make the assumption of smoothness between neighbouring spins orientations. Therefore, we have to recompute the partition function defined in the first equality of Eq. (20). But in this temperature regime, and since  $K = \frac{J}{k_B T}$  is inversely proportional to the temperature and therefore small, we can make a Taylor expansion of the exponential

$$e^x \approx 1 + x + \mathcal{O}(x^2) \quad (26)$$

Thus the partition function simplifies significantly, taking the form

$$\begin{aligned} \mathcal{Z} &= \int_{\text{accessible states}} e^{-\beta \mathcal{H}_{\text{state}}} \\ &= \int \mathcal{D}[\theta] e^{-\beta (-J \sum_{\langle i,j \rangle} \cos(\theta_i - \theta_j))} \\ &= \int \mathcal{D}[\theta] \prod_{\langle i,j \rangle} e^{K \cos(\theta_i - \theta_j)} \\ &\approx \int \mathcal{D}[\theta] \prod_{\langle i,j \rangle} [1 + K \cos(\theta_i - \theta_j) + \mathcal{O}(K^2)]. \end{aligned} \quad (27)$$

For the computation of the former partition function, we shall make use of the following

---

<sup>2</sup>Remember that this expression is not a general result as it was obtained under the assumptions of the XY-model and all results of the expected values are biased by this fact.

relationships

$$\int_0^{2\pi} \frac{d\theta_i}{2\pi} \cos(\theta_i - \theta_j) = 0, \quad (28a)$$

$$\int_0^{2\pi} \frac{d\theta_j}{2\pi} \cos(\theta_i - \theta_j) \cos(\theta_j - \theta_k) = \frac{1}{2} \cos(\theta_i - \theta_k), \quad (28b)$$

$$\int_0^{2\pi} \int_0^{2\pi} \frac{d\theta_i d\theta_j}{(2\pi)^2} \cos^2(\theta_i - \theta_j) = \frac{1}{2}. \quad (28c)$$

In order to settle down the notation, we shall explicitly compute the partition function of a  $2 \times 2$  spin configuration. We should consider all the possible accessible states of the system, taking into account that in the high-temperature regime we do not require that consecutive spins have similar angles. One of these states is sketched in Fig. 11, where we have numbered the spins from 1 to 4. As shown in Eq. (27), to compute the partition function we need to take the product among all possible pairs of first-neighbors, so

$$\begin{aligned} \mathcal{Z} &= \frac{1}{(2\pi)^4} \int_0^{2\pi} \int_0^{2\pi} \int_0^{2\pi} \int_0^{2\pi} [1 + K \cos(\theta_1 - \theta_2)] \cdot [1 + K \cos(\theta_1 - \theta_3)] \times \\ &\quad \cdot [1 + K \cos(\theta_2 - \theta_4)] \cdot [1 + K \cos(\theta_3 - \theta_4)] d\theta_1 d\theta_2 d\theta_3 d\theta_4 \\ &= \frac{1}{(2\pi)^4} \int_0^{2\pi} \int_0^{2\pi} \int_0^{2\pi} \int_0^{2\pi} [1 + K \cos(\theta_1 - \theta_2) + K \cos(\theta_1 - \theta_3) + K^2 \cos(\theta_1 - \theta_2) \cos(\theta_1 - \theta_3)] \times \\ &\quad \cdot [1 + K \cos(\theta_2 - \theta_4) + K \cos(\theta_3 - \theta_4) + K^2 \cos(\theta_2 - \theta_4) \cos(\theta_3 - \theta_4)] d\theta_1 d\theta_2 d\theta_3 d\theta_4. \end{aligned}$$

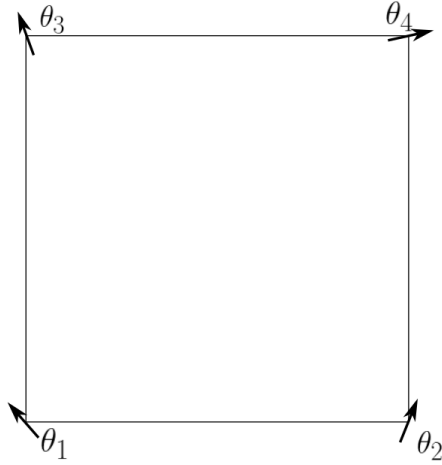


Figure 11: Cartoon of one of the accessible state of a  $(2 \times 2)$  spin matrix in the high temperature regime. Note how the change in direction of consecutive spins is not small.

Expanding the product we find that, out of the sixteen terms,

- One is the unity,
- There are four products of pair of cosines,
- There are four products of triplets of cosines,
- There is one product of quadruplets of cosines.

Following the rules of Eqs. (28a)-(28c), the products of singles, pairs and triplets vanish, while the product of quadruplets amounts to

$$\begin{aligned}
 & \frac{1}{(2\pi)^4} \int_0^{2\pi} \int_0^{2\pi} \int_0^{2\pi} \int_0^{2\pi} d\theta_1 d\theta_2 d\theta_3 d\theta_4 K^4 \cos(\theta_1 - \theta_2) \cos(\theta_1 - \theta_3) \cos(\theta_2 - \theta_4) \cos(\theta_3 - \theta_4) \\
 &= \frac{1}{(2\pi)^2} \int_0^{2\pi} \int_0^{2\pi} d\theta_2 d\theta_3 K^4 \left[ \frac{1}{2} \cos(\theta_2 - \theta_3) \right] \left[ \frac{1}{2} \cos(\theta_2 - \theta_3) \right] \\
 &= \frac{K^4}{4}.
 \end{aligned} \tag{29}$$

But this is a term that scales with  $K^4$ , and therefore negligible in the high-temperature regime. Thus, the only contribution that survives is the one coming from the unity in

the integrand and, therefore, we arrive to the conclusion that the partition function is normalized.

The next step, as we did in the previous Section in order to study the ordering of our system, is the computation of the correlation function,  $\langle \vec{S}_0 \cdot \vec{S}_{\mathbf{R}} \rangle = \langle \cos(\theta_0 - \theta_{\mathbf{R}}) \rangle$ . Hence all reduces to the computation of the following integral

$$\langle \cos(\theta_0 - \theta_{\mathbf{R}}) \rangle = \frac{1}{Z} \int \mathcal{D}[\theta] \cos(\theta_0 - \theta_{\mathbf{R}}) \prod_{\langle i,j \rangle} [1 + K \cos(\theta_i - \theta_j)] \quad (30)$$

The ideas for the computation of this integral are taken from Ref. (12) (pages 163-164). The mathematical foundations are based again on the well known relationships of Eqs. (28a)-(28c), and the main idea behind is that the only term that contributes to the correlation function corresponds to the shortest path (of length  $|\mathbf{R}|$ ) connecting the points  $\mathbf{0}$  and  $\mathbf{R}$ .

Again, before giving the general solution, we shall particularize the calculation for the  $(2 \times 2)$  example of Fig. 11. We are going to take  $\mathbf{R} = (1, 0)$ , i.e. one vector directed along the positive direction of the  $x$ -axis. As we did before in Sec. 5.1, we sweep over all the spins in the system, consider each of them as the origin and compute the dot product with the neighbour located at  $\mathbf{R}^3$ . In this example, this translates into

$$\begin{aligned} \langle \vec{S}_0 \cdot \vec{S}_{\mathbf{R}=\mathbf{x}} \rangle &= \frac{1}{(2\pi)^4} \int_0^{2\pi} \int_0^{2\pi} \int_0^{2\pi} \int_0^{2\pi} \cos(\theta_1 - \theta_2) \cdot [1 + K \cos(\theta_1 - \theta_2)] \cdot [1 + K \cos(\theta_1 - \theta_3)] \\ &\quad \cdot [1 + K \cos(\theta_2 - \theta_4)] [1 + K \cos(\theta_3 - \theta_4)] d\theta_1 d\theta_2 d\theta_3 d\theta_4. \end{aligned} \quad (31)$$

Now using the stated relationships for the cosine functions we notice that the non-zero terms are just

$$\begin{aligned} \langle \vec{S}_0 \cdot \vec{S}_{\mathbf{R}=\mathbf{x}} \rangle &= \frac{1}{(2\pi)^2} \int_0^{2\pi} \int_0^{2\pi} K \cos^2(\theta_1 - \theta_2) d\theta_1 d\theta_2 + \\ &\quad + \frac{1}{(2\pi)^4} \int_0^{2\pi} \int_0^{2\pi} \int_0^{2\pi} \int_0^{2\pi} K^3 \cos(\theta_1 - \theta_2) \cos(\theta_1 - \theta_3) \cos(\theta_3 - \theta_4) \cos(\theta_2 - \theta_4) d\theta_1 d\theta_2 d\theta_3 d\theta_4, \end{aligned}$$

where a simple inspection allow us to deduce that

---

<sup>3</sup>In fact, in this isotropic system where  $x$  and  $y$  are equivalent we can compute  $\|\mathbf{R}\| = 1$  and average the 4 spins. In other words, we can take four integrals like the one presented in Eq. (31), each of them considering the origin at one of the four spins. However all contributes with the same amount and thus the result of the average is the same as the one explicitly performed.

1. The former independent term in the computation of the partition functions, now vanishes since the integral of the cosine function is zero.
2. The two terms that survive corresponds to the possible paths connecting the two spins 1 and 2.
3. Every segment in the path contributes with a factor  $K/2$ .
4. The term that relates the spin 1 and 2 via  $K \cos(\theta_1 - \theta_2)$  corresponds with the shortest path between them and thus accounts for a value of  $\frac{K}{2}$ .
5. The path  $1 \rightarrow 3 \rightarrow 4 \rightarrow 2$  however accounts with a term  $\left(\frac{K}{2}\right)^3$ . In the high temperature regime, this contribution is negligible with respect the first contribution.

In summary, only the shortest path joining sites  $\mathbf{0}$  and  $\mathbf{R}$  account for the correlation function, because longer paths are weighted by higher powers of  $\frac{K}{2} = \frac{J}{2k_{\text{B}}T}$  which are small in the temperature regime that we are interested in.

Now, the previous results can be generalized, so the correlation function can be expressed as

$$\begin{aligned}
\langle \cos(\theta_{\mathbf{0}} - \theta_{\mathbf{R}}) \rangle &= \int_0^{2\pi} \dots \int_0^{2\pi} \frac{d\theta_{\mathbf{0}} \dots d\theta_{\mathbf{R}}}{(2\pi)^{R+1}} \cos(\theta_{\mathbf{0}} - \theta_{\mathbf{R}}) \times \\
&\quad [1 + K \cos(\theta_{\mathbf{0}} - \theta_{\mathbf{1}})] \dots [1 + K \cos(\theta_{\mathbf{R}-1} - \theta_{\mathbf{R}})] = \\
&= \left(\frac{K}{2}\right)^{|\mathbf{R}|} = e^{-\frac{|\mathbf{R}|}{\zeta}}, \tag{32}
\end{aligned}$$

where

$$\zeta = \frac{1}{\ln\left(\frac{2k_{\text{B}}T}{J}\right)} \tag{33}$$

is the correlation length, and  $|\mathbf{R}|$  represents the number of segments required to connect  $\mathbf{0}$  and  $\mathbf{R}$ . The most important conclusion is that the disordered high-temperature phase is characterized by an exponential decay of correlations (12).

As a final note, in general there might not be a unique path of length  $|\mathbf{R}|$  connecting both sites but multiple ones as it is depicted in Figure 12. If this happens it can be proved that the exponential decay still holds but with slightly different exponents.

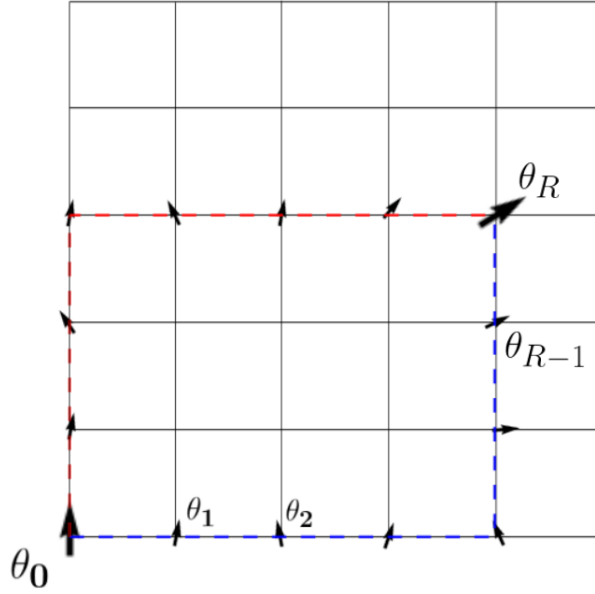


Figure 12: Sketch of two different graphs of length  $|\mathbf{R}|$  joining spins  $\theta_0$  and  $\theta_{\mathbf{R}}$

## 6 Berezinskii-Kosterlitz-Thouless transition

The results of the previous Sections do have profound implications on the physical behaviour of the system. To summarize the situation up to this point, let us recap the most important points:

- We are working in a two-dimensional problem with a Hamiltonian that only considers short-range (first-neighbour) interactions, and where the spins can point in any direction of the plane.
- The system presents an  $\mathcal{O}(2)$  continuous symmetry: if we modify the angle of rotations of all the rotors by the same amount, the energy is preserved.
- Due to the Mermin-Wagner theorem, we know that we cannot have an spontaneous symmetry breaking. That means that the macroscopic magnetization averages to zero at all temperatures.
- Despite this fact, the order of the system is very different in the low and in the high-temperature regime, as reflected by the spin-spin correlation function.
- At low-temperature, the correlation function decays as a power factor of the distance between the spins, so it goes to zero when  $|\mathbf{R}| \rightarrow \infty$  (the system is not in an ordered

state as Mermin-Wagner theorem stated). But this decay is not exponential, so the system is not in a fully disordered phase. The term “quasi-long-range order” was coined to refer to such states.

- In the high-temperature regime, there is an exponential decay of the spin-spin correlation function, so the system is in a fully disordered phase.

This difference in the ordering of the phases points to the existence of a new kind of phase transition, named as topological phase transitions or Berezinskii-Kosterlitz-Thouless (BKT) transitions in honour to its discoverers. There must be a finite temperature at which the ordering of the phase changes from the “quasi-long-range” to the disordered state, and this must happen without a change of the global order parameter (the magnetization), in contrast with the traditional first- or second-order phase transitions of the Landau theory. Such a phase transition was discovered by ...

## 6.1 Topological phase transition

The answers to why and where this transition occurs is related with the free energy of the vortex texture and how this affects the interaction between them. Recalling Eq. (6) and Eq. (12),  $E_{\text{vor}} = E_0 + \pi n^2 J \ln\left(\frac{L}{a}\right)$ , the energy of an isolated vortex presents a logarithmic divergence with the size of the system and, thus, vortices are not favoured at low temperatures.

However, at finite temperature, the energy is not the right thermodynamic potential to be minimized: we should turn our attention to the Helmholtz free energy,  $F$ , defined as

$$F = E - TS, \quad (34)$$

where  $S$  is the entropy of the system,

$$S = k_B \ln(\Omega), \quad (35)$$

and  $\Omega$  is the number of accessible states. If  $L$  is the system size and  $a$  is the spacing between neighbour spins, then there are  $\left(\frac{L}{a}\right)^2$  sites to locate the center of the vortices. Therefore<sup>4</sup>,  $S = k_B \ln\left(\frac{L}{a}\right)^2$  and, as a consequence, the free energy of a single vortex ( $n = 1$ ) amounts to

$$F = E_0 + (\pi J - 2k_B T) \ln\left(\frac{L}{a}\right), \quad (36)$$

where  $E_0$  is the constant term related with the ferromagnetic ordering. Very interestingly, for a  $2D$  system, the energy and the entropy presents the same logarithmic functional

---

<sup>4</sup>Is true that there are infinitely many type of vortices with the same energy. However, all of them are related by a phase and thus are the same up to a global symmetry operation of our Hamiltonian. This is why, only configurational entropy plays a role.

form with the system size. For  $T < \pi J/2k_B T$ , then the term in the parenthesis in Eq. (36) is positive, and the free energy diverges when  $L \rightarrow \infty$ . For  $T > \pi J/2k_B T$ , the term in the parenthesis in Eq. (36) is negative and the system can lower its free energy producing vortices. The critical temperature is located right at  $T_{\text{BKT}} = \frac{\pi J}{2k_B}$ , the so-called Berezinskii-Kosterlitz-Thouless temperature.

We can now relate this result with the asymptotic behaviours and the topology of the system. In the low temperature regime ( $T < T_{\text{BKT}}$ ) there exists a dependence between the spin textures. On the one hand free vortices are energetically unstable, on the other hand as we shown in Sec. 4 configurations consisting in vortex-antivortex pairs present a finite and thermodynamically stable energy in its equilibrium configuration (forming pairs of zero net vorticity) moreover they are consistent with the Mermin-Wagner theorem and are thus the only physical solution [see Eq. (17) and left panel of Fig. 13]. The pairs are topologically neutral, and from a large scale perspective, its orientational disturbance is canceled, allowing the appearance of the quasi-long-range ordered states.

However, in the high temperature regime ( $T > T_{\text{BKT}}$ ) the free vortices are favoured in terms of the free energy and become preferable to the bound pairs solution. Hence they can be stabilized independently and start to proliferate. The dependence between the different spin textures is not present any more, as the regions of the space with non-zero net vorticity become bigger the disorder of the system increases. The vortices start to unbind (see right panel of Fig. 13), increasing the entropy (disorder) and the distance between them, so the spin-spin correlation decays exponentially.

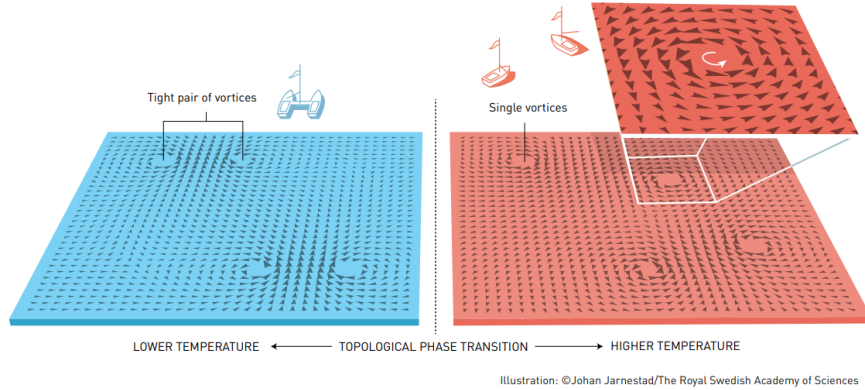


Figure 13: Intuitive representation of low and high temperature phases. Taken from the press release of the 2016 Nobel prize.

This phase transition is characterized by the sudden increase of the correlation length as reaching  $T_{\text{BKT}}$  from above. The correlation length can be defined for infinite systems as

$$\xi = - \lim_{r \rightarrow \infty} \frac{r}{\ln(C(r))}, \quad (37)$$

where we have momentarily change our notation to make it compatible with existing literature, and we have renamed the correlation function  $\langle \vec{S}_0 \cdot \vec{S}_{\mathbf{R}} \rangle$  so that  $C(r)$  stands for the correlation function. We can easily check that, within the high temperature regime, the correlation length defined in Eq. (37) is the same as the one that we obtained in

Eq. (33),  $\xi = \zeta = \frac{1}{\ln(\frac{2k_{\text{B}}T}{J})}$ , i.e. with the negative inverse of the coefficient in the

exponent of Eq.(32). Indeed,

$$\xi = - \lim_{r \rightarrow \infty} \frac{r}{\ln e^{-\frac{r}{\zeta}}} = \zeta$$

However in the low temperature regime the correlation length tends to infinite for infinite systems.

$$\xi = - \lim_{r \rightarrow \infty} \frac{r}{\frac{k_{\text{B}}T}{2\pi J} \ln(\frac{a}{r})} = +\infty$$

This divergence has been proved to be of the form  $\xi \approx e^{\frac{cte}{\sqrt{T - T_{\text{BKT}}}}}$  when reaching  $T_{\text{BKT}}$  from above (15) which shows a much faster evolution than the usually divergence  $|T - T_{\text{c}}|^{-\nu}$ , where  $T_{\text{c}}$  is the critical temperature, that characterize first or second order phase transitions mediating between ordered and disordered phases. Moreover the exponent of Eq. (25) typically labeled as  $\eta$  in the literature that characterizes the low temperature, quasi-long-range phase tends to

$$\eta_c = \frac{k_{\text{B}}T_{\text{BKT}}}{2\pi J} = \frac{k_{\text{B}}\pi J}{4\pi J k_{\text{B}}} = \frac{1}{4} \quad (38)$$

when approaching the transition temperature in accordance with (15).

As a final note, we would like to highlight the fact that in this phase transition there is no change in the order parameter -the average magnetization is preserved (equal to zero) during all the process- in contrast with what we are used in regular phase transitions. Moreover the entropy of our system changes smoothly ( $\mathcal{C}^\infty$ ) with the temperature in contrast with first (second) order phase transitions where discontinuities on the first (second) derivative of the Gibbs energy appear. That is why in some textbooks people refer to this transitions as infinite order in resemblance with Landau Theory although no change in the order parameter is perceived during the transition. In terms of topological properties the global vorticity of the system might change during the process and might be a fluctuating quantity in the high temperature regime, as we are supposing an infinite

plane our manifold is not compact and thus Poincaré-Hopf theorem do not restrict the value of the global vorticity. Although in the low temperature regime as a consequence of the compensation between vortex and anti-vortex textures we required a zero net vorticity in the high temperature regime this value might change. However, when we want to simulate this type of textures we are typically using periodic boundary conditions approaches where the global vorticity is restricted to be zero by Poincaré-Hopf theorem and hence must be constant in all the process.

## 7 Critical analysis of the XY-model

Up to now, we have restricted our study to the XY-model. It is important to keep in mind the assumptions on top of which we have been working on:

- A two-dimensional system where the rotors can point only in the directions contained in that plane.
- Continuous symmetry: the order parameter can rotate in a continuous way.
- Short-range interactions (a dipole interacts only with the first-neighbours).

In this section we shall revisit these assumptions and check whether they are essential for the existence of BKT-like transitions.

### 7.1 Influence of the short-range interactions

In the idealized XY-model studied above we are only taking into account the interaction with the nearest neighbours. However, in real magnetic (electric) systems, spins (dipoles) also interact via long-range dipole-dipole interaction that decays as the cube of the distance. This long range interaction significantly reduces the fluctuations. Indeed, it is expected that dipole-dipole interaction stabilizes the long range order against thermal fluctuations resulting in an spontaneously polarized ground state at low temperatures (16). Note that this do not enter in contradiction with the studied Mermin-Wagner theorem as the short-range interactions cannot be any longer assumed, being this one of the premises of the previous theorem. Despite the fact that at low temperatures the dipole-dipole interactions are crucial, it was found to become irrelevant in the high-temperature regime allowing for BKT transitions separating the ordered and disordered phases (17; 18; 19).

### 7.2 Influence of the continuous symmetry

A similar behaviour is found when dealing with two dimensional  $\mathbb{Z}_p$ -clock models. In these systems, spins can point along  $p$  directions distributed uniformly, that is

$$\theta_i = \frac{2\pi n_i}{p}, \text{ where } n_i = 0, \dots, p-1, \quad (39)$$

when  $p = 2$  we recover the Ising Model, and when  $p \rightarrow \infty$  we recuperate the XY-model. Ortiz and coworkers have shown how if  $p \leq 4$  only a second-order phase transition between the ordered and the disordered phase can be observed, as we are used to with the Ising model (20). However, for  $p \geq 5$  there exists an intermediate phase separating the ferromagnetic and paramagnetic ones characterized by its BKT behaviour (20). As  $p$  increases, the temperature at which the ferromagnetic order disappear decreases and in the limit when  $p \rightarrow \infty$  it becomes 0, consistently with the Mermin-Wagner theorem.

### 7.3 Influence of the dimensionality of the order parameter

Before entering in the dimensionality of the system we would like to make some comments about the importance of the topology of our order parameter space and how it might influence the kind of defects and the physics of the system. In order to study the topology of our order parameter we typically make use of algebraic topology tools like Homotopy groups. If the reader wants to go deeper he can consult (21) Part II. However, we shall give now some intuitive basic ideas that will help to better understand what follows.

Algebraic topology associates to each topological space  $\mathcal{X}$  some groups in such a way that if two topological spaces are homeomorphic (i.e equivalent up to continuous transformations) their associated groups will be identical. This relation allows us to differentiate two spaces always that their associated groups differ. Homotopy groups, usually labeled as  $\pi_n(\mathcal{X})$  serves us hence to classify topological spaces.  $\pi_0(\mathcal{X})$  measures the number of connected components of our topological space  $\pi_1(\mathcal{X})$  somehow measures “the number of holes” of our space but in general  $\pi_n(\mathcal{X})$  is the set of classes of applications from the n-sphere ( $\mathbb{S}^n$ ) to our topological space. To illustrate this, see Fig. 14, and its relation to the calculation of the first homotopy group  $\pi_1(\mathcal{X})$ . In the Sphere every loop (we can identify a loop with a circumference  $\mathbb{S}^1$  immersed on the topological space) can be contracted to one point which means that all applications belong to the same class and thus  $\pi_1(\mathbb{S}^2) = 1$  whereas in the Torus as it has holes magenta and red loops are different and different from the constant one (we cannot transform one to another), moreover it is different if the red (or magenta) loop makes one or more turns to the torus and thus  $\pi_1(\mathbb{S}^2) = \mathbb{Z} \times \mathbb{Z}$  which proves that the sphere and the torus are not homeomorphic since their first homotopy groups differ. Notice that  $\pi_0(\mathbb{S}^2) = \pi_0(\mathbb{T}^2) \cong 1$  since both spaces are path connected, this reinforces the fact that shearing some homotopy groups do not imply that the spaces are homeomorphic but finding one differing group suffices to distinguish between them.

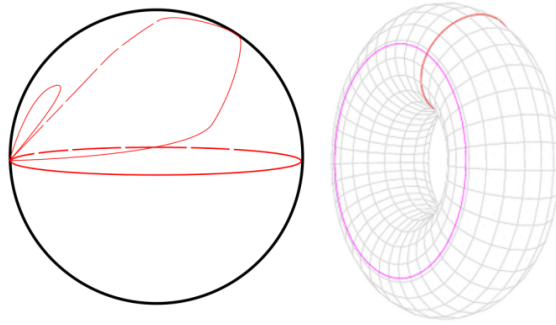


Figure 14: Consecutive transformations of a given loop in the sphere ( $\mathbb{S}^2$ ) that shows how every loop can be continuously contracted to a point whereas in the Torus ( $\mathbb{T}^2$ ) red and magenta loops are non homotopic and represent the generators of its first homotopy group. Image taken from Wikipedia.

### 7.3.1 One dimensional order parameter

After this brief introduction we shall start with the simplest model revised in this work: the Ising model. Within its framework, the order parameter is one dimensional and its topological space  $\mathcal{X}$  can be easily identified with two disconnected points (i.e. up and down polarization). Hence, the first nontrivial homotopy group is  $\pi_0(\mathcal{X}) \cong \mathbb{Z}_2$  (remember that  $\mathbb{Z}_2$  is the group formed by +1 and -1 with the product).

This implies that one-dimensional defects (if we are in a two dimensional space) such as domain walls cannot be continuously deformed into a mono-domain structure. In the Ising model, a second-order phase transition occurs between the ferro and para-magnetic states.

### 7.3.2 Two dimensional order parameter

In contrast, in the XY-model where the order parameter is two-dimensional and the order parameter space as commented before can be identified with a unit circumference ( $\mathbb{S}^1$ ),  $\pi_0(\mathbb{S}^1)$  becomes trivial as the space is path-connected and the first nontrivial homotopy group is  $\pi_1(\mathbb{S}^1) \cong \mathbb{Z}$ . This implies that one-dimensional defects are no longer topologically stable and can be continuously deformed to a mono-domain whereas vortices become important and are the topologically protected zero-dimensional defects of our system. The physics has already been studied in detail no first-order nor second-order phase transition is observed but a BKT-like one.

### 7.3.3 Three dimensional order parameter

Last but not least if we increase the dimensionality of the order parameter again and let spins point in any direction of the space. Following Ref. (22), we shall assume that our order-parameter's texture can be described using a vector field of the form

$$\mathbf{S}(\mathbf{r}) = (\cos \Phi(\phi) \sin \Theta(r), \sin \Phi(\phi) \sin \Theta(r), \cos \Theta(r)), \quad (40)$$

where  $\mathbf{S}(\mathbf{r})$  is a normalised  $3D$  vector defined in a  $2D$  space, and  $\Phi(\phi)$  and  $\Theta(r)$  are functions of the azimuthal angle  $\phi$  and distance  $r$  [polar coordinates that describe the position  $\mathbf{r} = (r \cos \phi, r \sin \phi)$  where the local spin is located]. Particular functional forms will depend on the specific pattern to be described, and some typical shapes for vortices (top row,  $m = 1$ ) and antivortices (bottom row,  $m = -1$ ) are shown in Fig. 15.

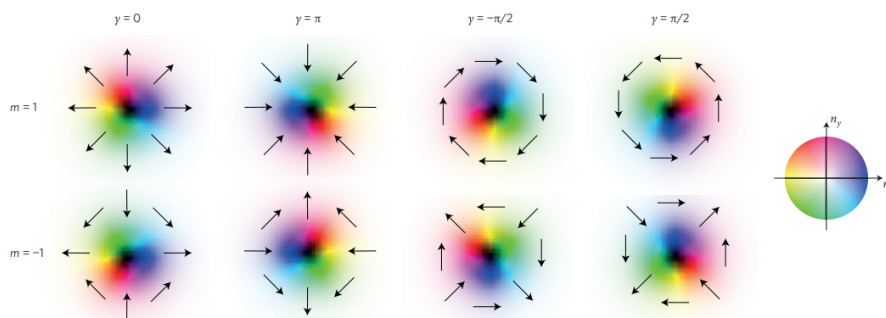


Figure 15: Different dipole patterns classified by the vorticity of the core  $m$ , and the angle that the dipole located at the rightmost-position form with the  $x$  axis,  $\gamma$ , referred to as the helicity in Ref. (22). These patterns are obtained assuming that  $\Phi(\phi) = m\phi + \gamma$  in Eq. (40). Only the in-plane components of the local dipoles are shown, with the color indicating a particular direction as shown in the circle at the right. In order to have a skyrmion structure, the out-of-plane component of the polarization must change between the periphery and the core. This change will depend on how the function  $\Theta(r)$  will be defined, assuming the appropriate fixed boundary conditions at  $r \rightarrow \infty$  and  $r = 0$ . Adapted from Ref. (22)

This model is known as the planar Heisenberg model. Its order parameter can be identify with a unit sphere ( $\mathbb{S}^2$ ). Since this unit sphere is simply-connected, it fulfills that  $\pi_0(\mathbb{S}^2)$  and  $\pi_1(\mathbb{S}^2)$  are trivial, and the first non trivial homotopy group is  $\pi_2(\mathbb{S}^2) \cong \mathbb{Z}$ . With this topology, domain-walls and vortices can both be continuously deformed to mono-domain structures and are trivial. Therefore, the skyrmion texture turn to be the first topologically stable structures.

In order to understand the physics of such a system, we shall perform a similar analysis as we did for the case of the XY-model to derive the Hamiltonian for the system under the assumption of small fluctuations. First, we compute the product of neighbouring spins

$$\mathbf{S}_i \cdot \mathbf{S}_j = \sin(\Theta_i) \sin(\Theta_j) [\cos(\Phi_i) \cos(\Phi_j) + \sin(\Phi_i) \sin(\Phi_j)] + \cos(\Theta_i) \cos(\Theta_j).$$

Using now the trigonometric relationships  $\cos(a - b) = \cos(a) \cos(b) + \sin(a) \sin(b)$ ,

$$\mathbf{S}_i \cdot \mathbf{S}_j = \sin(\Theta_i) \sin(\Theta_j) \cos(\Phi_i - \Phi_j) + \cos(\Theta_i) \cos(\Theta_j).$$

And assuming a smooth behaviour of  $\Phi$ , then the cosine can be approximated by the Taylor expansion  $\cos(x) \approx 1 - \frac{x^2}{2}$ ,

$$\mathbf{S}_i \cdot \mathbf{S}_j \approx \sin(\Theta_i) \sin(\Theta_j) + \cos(\Theta_i) \cos(\Theta_j) - \sin(\Theta_i) \sin(\Theta_j) \frac{(\Phi_i - \Phi_j)^2}{2}.$$

Working in the same way with  $\Theta$ , we get

$$\mathbf{S}_i \cdot \mathbf{S}_j \approx 1 - \frac{(\Theta_i - \Theta_j)^2}{2} - \sin^2(\Theta_i) \frac{(\Phi_i - \Phi_j)^2}{2}.$$

Finally, taking the continuum limit, following the reasoning of Eq.(3)-Eq.(6), we finally arrive to

$$\mathcal{H} = -2NJ + \frac{J}{2} \iint dx dy [(\nabla\Theta)^2 + \sin^2(\Theta)(\nabla\Phi)^2]. \quad (41)$$

Because of the symmetry of the problem it is interesting to introduce polar coordinates, which as the reader know satisfy

$$\begin{aligned} x &= r \cos(\phi), \\ y &= r \sin(\phi), \\ r &= \sqrt{x^2 + y^2}, \\ \phi &= \arctan\left(\frac{y}{x}\right), \\ dxdy &= r dr d\phi. \end{aligned}$$

As an example, we can compute the energy of one of the skyrmionic patterns shown in Fig. 15. More precisely, the first pattern of the top row ( $m = 1$ ,  $\gamma = 0$ ), where  $\Phi = \phi$ . For  $\Theta(r)$  we can choose a smooth function that vanishes at the origin [so  $\cos(\Theta) = 1$

and according to Eq. (40) the out-of-plane component of the dipole points in the positive direction at the core] and equals  $\Theta(r) = \pi$  when  $r \rightarrow L$  [so  $\cos(\Theta) = -1$  and according to Eq. (40) the out-of-plane component of the dipole points in the negative direction at the periphery]. The most simple function is given by the linear relation  $\Theta(r) = \frac{\pi}{L}r$ . Then, we can perform the integral of Eq. (41) passing to a polar coordinate system

$$\begin{aligned}
\mathcal{H} &= -2NJ + \frac{J}{2} \int_0^L \int_0^{2\pi} r dr d\phi \left[ \left( \frac{\partial \Theta}{\partial r} \right)^2 + \frac{\sin^2 \Theta}{r^2} \right] \\
&= -2NJ + \pi J \int_0^L r dr \left( \frac{\partial \Theta}{\partial r} \right)^2 + 2\pi J \int_0^L \frac{\sin^2 \Theta}{r} dr \\
&= -2NJ + \pi^3 J + 2\pi J \int_0^\pi \frac{\sin^2 x}{x} dx \\
&= -2NJ + \pi^3 \frac{J}{2} + \pi J \cdot 1.21883.
\end{aligned} \tag{42}$$

The last integral has been computed numerically, after the change of variables  $\frac{\pi}{L}r = x$ .

The most important result is that the energy given in Eq. (42) is finite and independent of the size of the system, in contrast with the energy of a single vortex [Eq. (12)] that presented a logarithmic divergence with  $L$ . If we now compute the Helmholtz free energy [ $F = E - TS$ , Eq. (34)], and since the entropy term still diverges logarithmically with the size of the system,  $F$  will diverge towards  $-\infty$  at any temperature in the macroscopic limit. Therefore, the system is always in a disordered state and no phase transition is observed as a function of the temperature. This result is in complete agreement with the treatment of the Heisenberg model in Chapter 6.6 of Ref. (23).

## 7.4 Influence of the dimensionality of the system

As a final note we would like to treat the dimensionality of the system. Up to now, we have assumed that the spinors live in a 2D-plane, although the order parameter was allowed to point in any direction in the previous section. But, what would happen if the spinors can be centered in a given point of a 3D-space?

Revising Sec. 6.1 we can see that the logarithmic dependence of the energy with the system size is essential in order to have a topological phase transition of BKT type. Assuming any other dependency of the energy with the system size will result in either:

- Having active vortices at all temperatures, in the case where  $E_{\text{vor}} = \text{constant} < \infty$ ,
- Not having vortices at any temperature, in the case where  $E_{\text{vor}} \propto L^x$  with  $x \geq 0$ .

Therefore, as this logarithmic dependence of the energy with the system size is inherent to the two dimensionality of the problem, suggest that BKT transitions are elusive in more dimensions. In fact the quasi-long-range phase is nonexistent in the model when embedded in three dimensions see for example Eq. (6.1.21) of Ref. (11) or Eq. (22) of Ref. (24) where they saw that for large distances ( $r \rightarrow \infty$ ) the correlation function goes like

$$C(r) = \begin{cases} \left(\frac{L}{r}\right)^{\frac{T}{2\pi J}} & \text{if } d = 2 \\ e^{-CT} & \text{if } d \geq 3 \end{cases}$$

where  $C$  is a constant. There we can see that the quasi-long-range ordering is replaced by a long range order where correlation decays to a constant for large distances.

However, in a recent work by Nahas and coworkers in Ref. (25; 26) a BKT-like transition is observed in a low-dimensional ferroelectrics, despite many of the prerequisites that we have assumed for its existence do not hold. In particular:

- The dimensionality of the system (a 3D structure, although in a thin film geometry).
- The anisotropy of the interaction, so the system does not present the equivalent to the  $\mathcal{O}(2)$  continuous symmetry for the 3D-structure.
- The existence of long-range dipole-dipole interactions.

In Ref. (25), the authors performed Monte Carlo simulations of a system composed of  $L \times L \times h$  supercells of BaTiO<sub>3</sub>, periodically repeated along  $x$ - $y$  directions and finite along the  $z$  direction. The films were assumed to be under a tensile strain of 3%, mimicking the effect of a substrate with a notably larger lattice parameter. This tensile strain is known to favour an in-plane polarization of BaTiO<sub>3</sub>, pointing along the [110] direction. Simulations were carried out under open-circuit electrical boundary conditions. Therefore, a depolarizing field would appear if a net polarization is present along the [001] pseudocubic direction. Thus, the electrostatic boundary conditions also preclude the appearance of an out-of-plane component of the polarization. The supercell with  $h = 3$  unit cells and  $L = 30$  unit cells is depicted in Fig. 16.

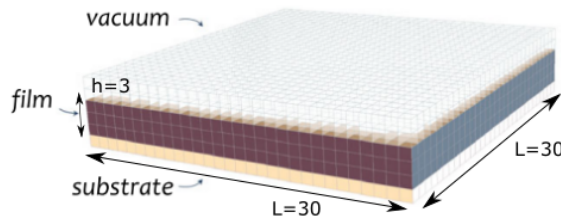


Figure 16: Sketch of the simulation supercell used in Ref. (25). Periodic boundary conditions are assumed in the  $(x, y)$  plane. Reprinted with permission from (25)

At low temperature, the system was ferroelectric with the local dipole moments confined to the film plane, so the macroscopic spontaneous polarization lie along the  $\langle 110 \rangle$  pseudocubic direction as they show in the symmetrized polarization pattern Fig. 17. Very interestingly, it was found how under the previous conditions the contribution of the interplane coupling to the total energy of the system was very small (below 4%). This fact implies no correlation between electric dipoles belonging to different planes, and allows the treatment of the system as effectively two-dimensional. In the high temperature phase (above the Curie temperature of  $T_C \approx 539$  K) the system is paraelectric (i.e. disordered), with a rapid exponential decay of the correlation function.

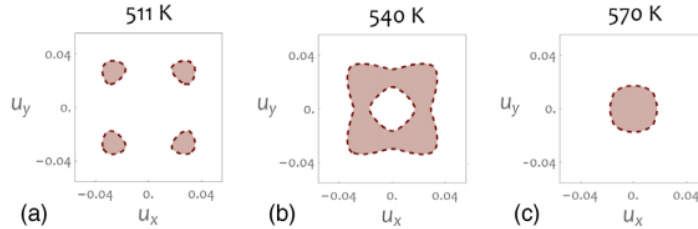


Figure 17: Temperature evolution of the symmetrized in-plane polarization pattern. Reprinted with permission from (25).

The key point of Ref. (25) is that the phase transition between the ferroelectric and the paraelectric phase is mediated by a phase with quasi-long-range order. Moreover in the previous work the authors could fit the transition to a BKT behaviour, illustrating most of the theory developed until now in this work. In particular, the dipole-dipole correlation function  $C(r)$  described in Eq. (18) was computed at different temperatures (see the insets of Fig. 18) and the functional form was fitted to a power law algebraic function [Eq. (25)] and to an exponential function [Eq. (32)]. From the fittings, the values of critical exponents  $\eta$  and  $\xi$  can be extracted as a function of temperature (Fig. 18) .

based on scaling analysis techniques, they could detect that this critical phase extended up to  $T_{BKT} = 545$  K where the BKT transition occurs. In Fig. 18 we can see the fits to a power law and an exponential decay depending on the temperature regime and how critical exponents vary as a function of the temperature.

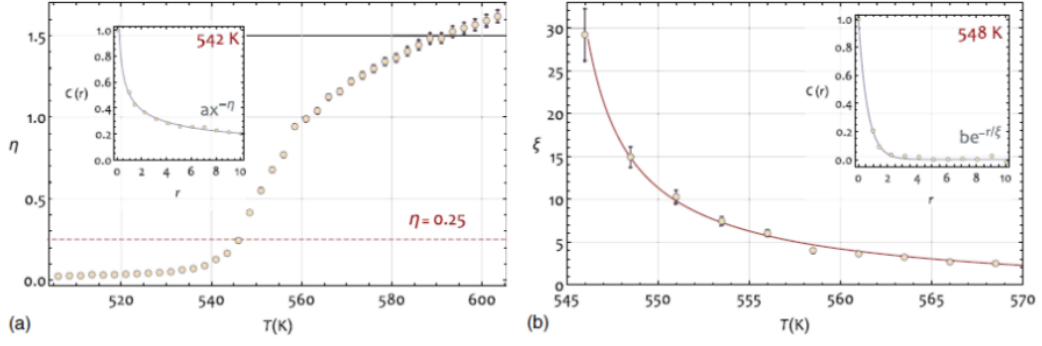


Figure 18: Evolution of the critical exponents  $\eta$  and  $\xi$  with temperature obtained by a fit to a power-law decay as specified in the inset of (a) or a exponential one as in the inset of (b). Red line in (b) corresponds to an exponential fit to the data as predicted for the divergence of the correlation length. Figure reprinted with permission from Ref. (25).

In Fig. 18 we can clearly distinguish both, low-temperature and high-temperature regimes characterized by the quasi-long-range power-law decay and the disordered exponential decay respectively. Moreover we can distinguish different behaviours for the critical exponents near  $T_{\text{BKT}}$  observing the announced tendency in Eq. (38) of  $\eta = \frac{1}{4}$  when we approach the transition temperature, and the exponential divergence of  $\xi$  when reaching it from above. All these features suggest that this transition is of BKT type, as it was confirmed when the authors could observe that the mechanism of the transition was the unbinding of vortex-antivortex pairs illustrated in the plot of Fig. 19

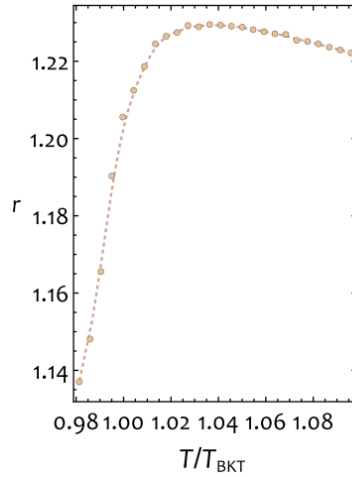


Figure 19: Evolution of the average vortex-antivortex pair distance as a function of the temperature. Figure reprinted with permission from Ref. (25).

As we can observe as we approach to the transition temperature the distance between vortex and antivortex increase as they start to unbind. The consequent decay is due to the finitude of the system and the increasing number of defects in it.

## 8 Topological phase transitions in $\text{PbTiO}_3/\text{SrTiO}_3$ superlattices.

Up to this point we have explored the basics of the BKT theory within the framework of the XY-model. We have also relaxed some of the hypothesis required for the appearance of this type of transitions, allowing them to be present in some systems *prima facie* unexpected. Guided by these theoretical results (25; 26) that prove the possibility of finding BKT behaviour in thin ferroelectric films, together with recent experimental results by Ghosh *et al.* (27) that suggest its existence in larger  $(\text{PbTiO}_3)_{20}/(\text{SrTiO}_3)_{20}$  superlattices, we have proceeded to explore the eventual existence of BKT transitions in  $\text{PbTiO}_3/\text{SrTiO}_3$  superlattices, similar to the ones studied in Ref. (28). We have carried out second-principles simulations, summarized in Appendix D, to explore two different scenarios.

The model was formed from the pure  $\text{PbTiO}_3$  (PTO),  $\text{SrTiO}_3$  (STO) models treated in (29) and averaging the interaction to treat the interfaces. In this way we constructed two different models with subtle differences between them that differ much in their physical response:

1. A system where the polarization in the  $\text{PbTiO}_3$  layers is confined to the  $xy$ -plane. Physically, this corresponds to a situation where the superlattice is under a tensile epitaxial strain that induces a polarization in the  $xy$  plane and prevents the formation of an out-of-plane polarization along the  $z$  direction. This model resembles the studies of Refs. (25; 26), and is characterized by a monodomain phase with polarization lying along  $[110]_{pc}$  direction in its equilibrium low temperature phase. From the computational point of view, a periodically repeated supercell made of  $10 \times 10 \times 20$  unit cells along  $x$ ,  $y$ , and  $z$  directions, respectively, is used with a slightly expansive strain in the plane of 0.5%.
2. A system where the polarization forms polarization vortices, as requested by the electrostatic constraint of having no polarization charges, i.e.  $\nabla \cdot \vec{p}_{\text{local}} = 0$  everywhere. Here, the local polarization can point along the three spatial directions. This model resembles the experimental situation found in Ref. (30; 28) and whose topological phase transitions are analyzed in Ref. (27). In both cases, the superlattices are grown on top of a  $\text{DyScO}_3$  substrate. From the computational point of view, a periodically repeated supercell made of  $20 \times 10 \times 20$  unit cells along  $x$ ,  $y$ , and  $z$  directions, respectively, is used.

## 8.1 First Model: polarization lying in the $xy$ plane.

Inspired by the results of Nahas *et al.* that predicted the existence of BKT phases in ferroelectrics, we tried to mimic the calculations done in Refs. (25; 26) with our first model constituted by a  $10 \times 10 \times 20$  supercell as explained before.

In our exploratory calculations, we have carried out 10000 Monte Carlo sweeps per calculation (as explained in Appendix D) and temperature steps of 20K to perform the sampling. Further calculations, with a more refined statistical samplings have been postponed to a subsequent publication.

The  $T = 0$  K equilibrium phase found after performing an annealing starting from a monodomain lying along  $[110]_{pc}$  (pc stands for pseudocubic) direction phase is presented in Fig. 20.

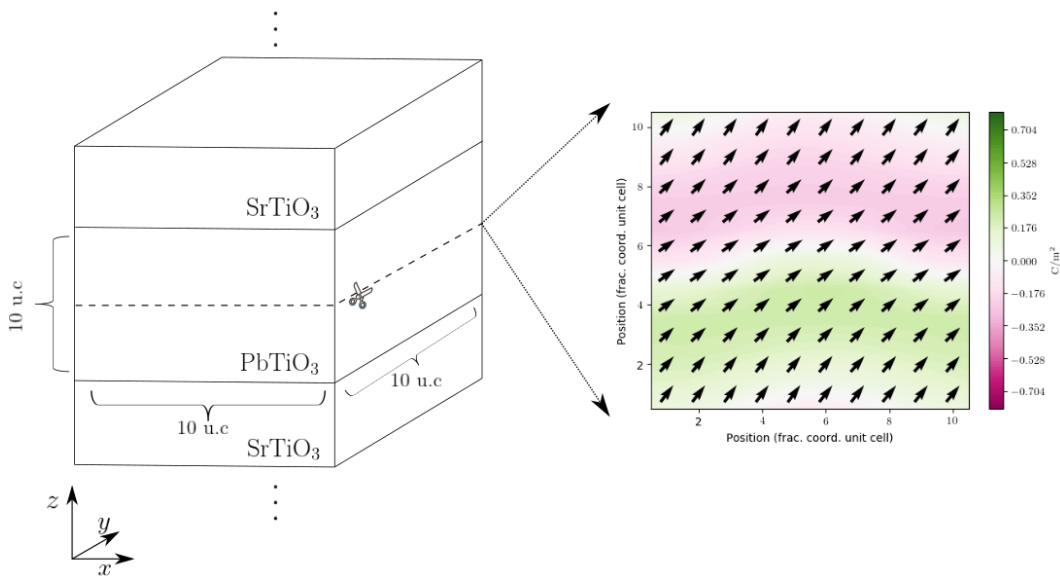


Figure 20: Section representing the local polarization at a central  $xy$ -plane of the  $\text{PbTiO}_3$  layer as schematized in the figure, at zero temperature after annealing. The arrows represent the in-plane ( $xy$ ) components of the polarization, while the colors refer to the out-of-plane component of the polarization ( $p_z$ ), perpendicular to the plane of the screen.

As we can observe, the zero temperature phase corresponds to a monodomain phase, with the polarization direction along the  $[110]_{pc}$  direction. The out-of-plane component of the polarization  $p_z$  is much smaller than the  $p_x$ ,  $p_y$  components, as it can be shown in  $y$  section of the polarization presented in Fig. 21, allowing thus to treat the order parameter as effectively two-dimensional.

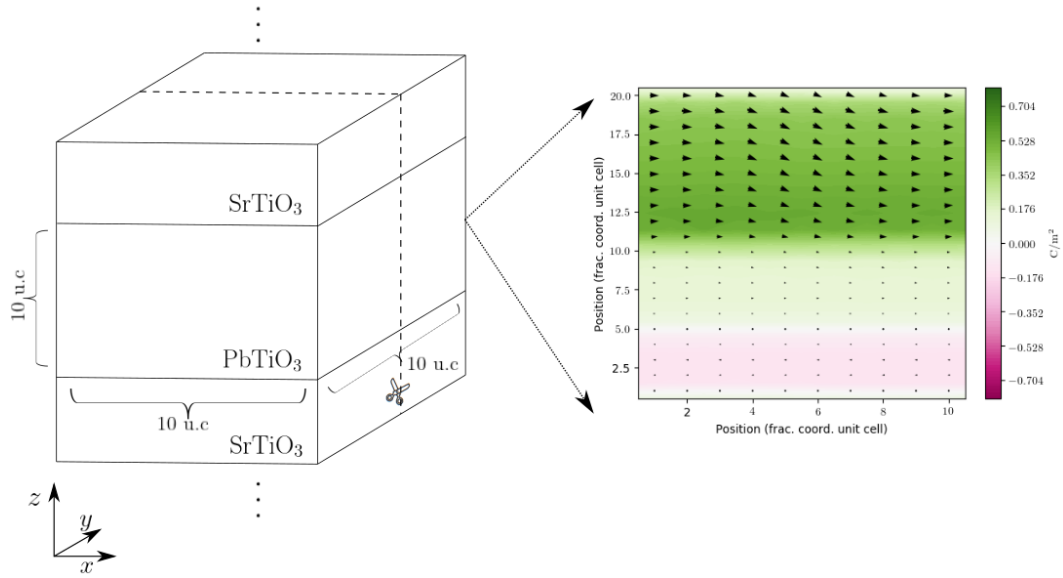


Figure 21: Section representing the local polarization in a  $xz$  plane as schematized in the figure at zero temperature found from the annealing. The arrows represent the in-plane ( $xz$ ) components of the polarization, while the colors refer to the component of the polarization perpendicular to the plane of the screen,  $p_y$ . Note how the color scale in the  $\text{PbTiO}_3$  layer is much darker here, compared to Fig. 20.

Due to long range dipole-dipole interactions, this ferroelectric phase is stable at low enough temperatures, as it happened in Ref. (25). The reader has to remember that the fingerprint for an ordered phase is a finite value of the correlation function as a function of the distance. A pure ferroelectrically ordered material would have a correlation function equal to one for any distance. In fact, the phase discussed here is present in our calculations up to  $T \approx 120 \sim 140K$ , where correlations as a function of the distance in the  $xy$  plane are above 0.85, as shown in Fig. 22.

In order to obtain the correlation function we computed the dipole-dipole product at a given distance and mediated over all the possible  $z$ -planes. Since the distance between unit cells is discrete, so are the points where we can compute the correlation function. The distance to the first-neighbour is 1 unit cell (u.c), the second neighbour is located at  $\sqrt{2}$  u.c. and so on.

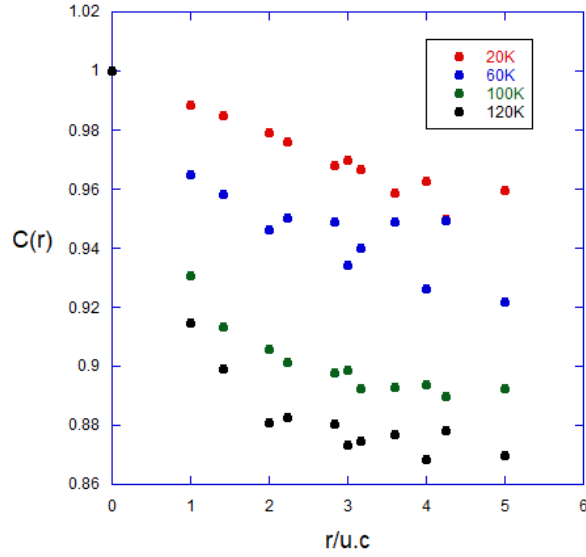


Figure 22: Correlation function for the dipoles in the  $xy$  plane as a function of the distance (in unit cells) at different temperatures (see legend). In this range of temperatures the  $\text{PbTiO}_3$  layer is in a monodomain ferroelectric phase, and the correlation function is high even at far distances.

If the temperature is further increased, the dipoles start to cant and to acquire certain disorder. Indeed, within this model, we can identify a range of temperatures between 140 and 240 K where the correlations as a function of the distance in the plane decays as a power law, as shown in Fig. 23.

and we can attribute it to a BKT-like behaviour. In Fig. 23 we show this regime that extends up to around  $T \approx 220 \sim 240\text{K}$ .

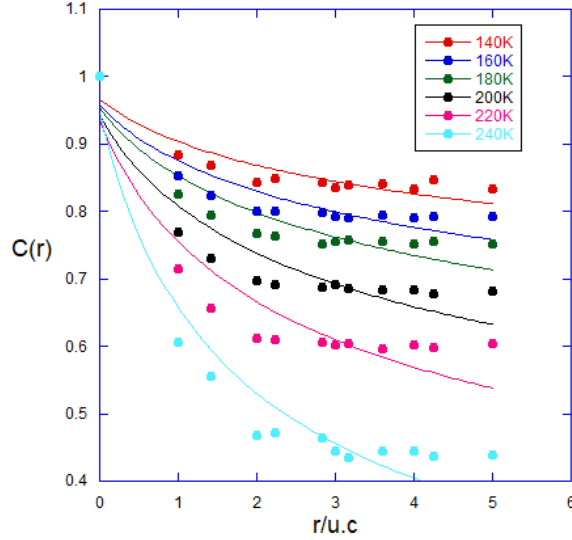


Figure 23: Correlation function for the dipoles in the  $xy$  plane as a function of the distance (in unit cells) at different temperatures (see legend). In this range of temperatures the correlation function decays as a power law,  $C(r) = a_0(r + 1)^{-\eta}$ , as in Eq. (25)<sup>5</sup>. The fit to this functional form is plotted as solid lines.

As we can draw from Fig. 23, the power-law fit captures the behaviour of the simulated data with regression coefficients larger than 0.93 for all cases. In Table 1 we show the evolution of the exponent  $\eta$  as a function of the temperature.

$T(K)$	$a_0$	$\eta$	$\mathbb{R}$
140	$0.967 \pm 0.016$	$0.098 \pm 0.013$	0.931
160	$0.96 \pm 0.02$	$0.130 \pm 0.017$	0.930
180	$0.95 \pm 0.02$	$0.16 \pm 0.02$	0.929
200	$0.95 \pm 0.03$	$0.22 \pm 0.02$	0.929
220	$0.94 \pm 0.04$	$0.31 \pm 0.04$	0.930
240	$0.95 \pm 0.04$	$0.53 \pm 0.04$	0.967

Table 1: Results obtained for the prefactor  $a_0$ , exponent  $\eta$ , and regression coefficient  $\mathbb{R}$ , as a function of temperature after performing the fit of the data plotted in Fig. 23 to the power-law functional form,  $C(r) = a_0(r + 1)^{-\eta}$ .

<sup>5</sup>In order to avoid a divergence when  $r = 0$ , and due to the fact that the autocorrelation function should be one, we have made the change  $r \rightsquigarrow r + 1$ . However the shape of the decay does not vary with respect to the one deduced in Sec. 5.2.

Finally, if we continue increasing the temperature this quasi-long-range ordered phase disappears, as expected by the theory, and a disordered one characterized by the exponential decay of the correlation function starts to proliferate. In Fig. 24 we show the abrupt change with the previous behaviour and how the correlation function fits to an exponential decay with a regression coefficient larger than  $\mathbb{R} = 0.99$  for the two temperatures computed ( $T = 260$  K and  $T = 280$  K).

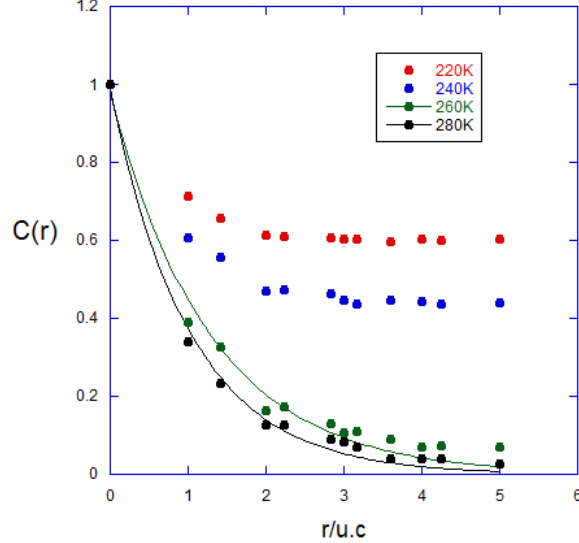


Figure 24: Correlation function for the dipoles in the  $xy$  plane as a function of the distance (in unit cells) at different temperatures (see legend). In this range of temperatures the correlation function decays exponentially,  $C(r) = a_0 e^{-r/\xi}$ , as in Eq. (32). The fit to this functional form is plotted as solid lines.

This transition is also reflected in the polarization pattern. In Fig. 25 we can see two polarization patterns of  $xy$  slices at a central plane of the  $\text{PbTiO}_3$  layer at different temperatures, corresponding to the QLRO and the disordered phases near the critical transition temperature.

On the one hand, in the low temperature regime, Fig. 25 (a), we can see that there are no spatially resolved defects, instead we have combined vortex anti-vortex textures that induce a certain canting of the spins. Nevertheless, we can still detect certain order at low distances.

On the other hand, in the high-temperature regime, Fig. 25 (b), defects start to unbind and they can be spatially resolved provoking that the polarization pattern is completely messed up as there is no cancellation of topological disorder and we can no

longer distinguish any preferred direction. This indicates that the transition temperature should be around  $T = 220K$  where the coefficient  $\eta = 0.31 \pm 0.04$  is in relative good agreement with the theoretical 0.25 predicted by the XY-model (a refinement of the calculations for a better agreement with the theoretical model is under development).

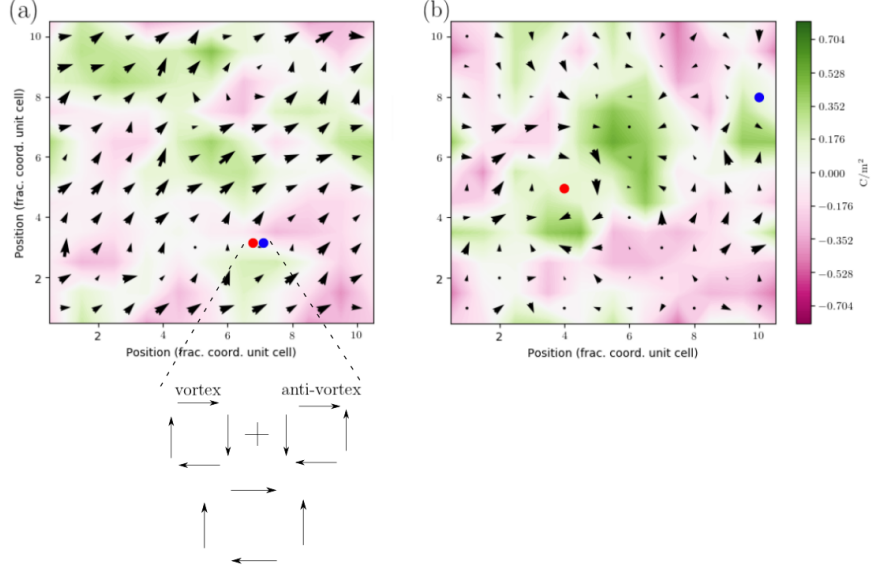


Figure 25: Polarization patterns along a  $xy$  plane at the center of the  $\text{PbTiO}_3$  layer at different temperatures:  $T = 220K$  (a) and  $T = 240K$  (b). Red dots stand for vortex textures whereas blue dots stands for anti-vortex textures. When we do not have spatially resolved defects (a) vortex and anti-vortex singularities cancel out and computing the vorticity as we learned in Fig. 3 around the singularity gives a result of  $n = 0$  as schematized by the sum of the vortex and anti-vortex textures below (a) panel.

## 8.2 Second Model: vortex textures in the polarization pattern

In this second model we tried to reproduce the experimental results found by A. Ghosh *et al.* The simulation box used was made of a  $20 \times 10 \times 20$  supercell, periodically repeated in space, as explained before. The in-plane lattice constant assumed in our calculations was  $3.901 \text{ \AA}$ .

First of all, and as in the previous case, we have performed an annealing in order to obtain the ground state of the system at zero temperature. The starting point for this relaxation was a configuration of  $180^\circ$  Ising-like domains lying along the  $[001]_{\text{pc}}$  direction. After the annealing, the system presented a phase composed by a sequence of alternating

clock-wise, counter-clock-wise array of vortices arranged along the  $[100]_{\text{pc}}$  direction, such as those previously discussed in Ref. (30; 28). The dipoles rotate in the  $xz$  planes. Any section cut along the  $y$ -direction shows the same structure. This relaxed structure is schematized in Fig. 26. As it already happened with the previous model, the aims of the calculations carried out in this work are explorative, with the same statistical quality as before.

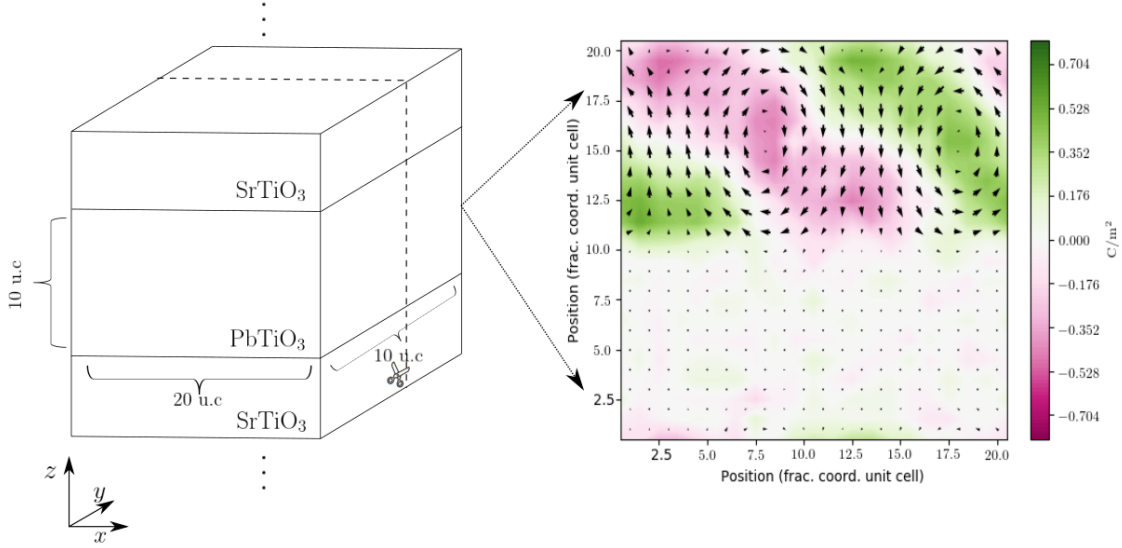


Figure 26: A section of the ground state of the system at zero temperature found from the annealing, for a particular  $y$ -plane. Arrows represent the in-plane components of the polarization in the  $xz$  plane. The color map represents the axial component of the polarization profile ( $p_y$ ).

The first two clear differences with respect to the results obtained by Nahas *et al.* in Ref. (25; 26), and by the those previously analyzed in Sec.8.1 are:

- The large coupling of the polarization along parallel  $y$ -planes. This is easy to check studying the correlation function between spins as a function of the distance in the  $y$ -direction and checking that it remains close to one independently of the distance. This fact implies that  $y$ -planes are correlated, and thus coupled, even for high temperatures as we can see in Fig 27. There we can see that even for  $T = 70 K$  the correlation between planes is high and we are hence facing a truly 3D system with a 3D order parameter.

- The fact that our polarization pattern is three dimensional, preventing vortices to be topologically stable defects is obvious just by looking at the polarization profile and noticing how the axial component of the polarization is of the same magnitude as the in-plane components.

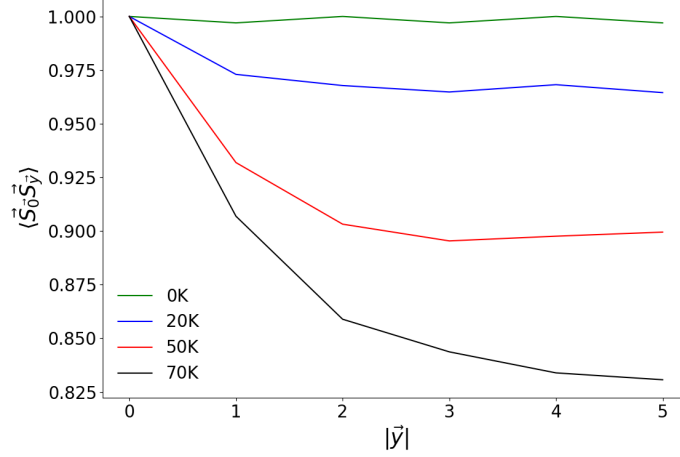


Figure 27: Correlation function between  $y$  planes at different temperatures, as specified in the legend. Here, we have computed the dipole-dipole product at two different sites shearing the same  $(x, z)$  coordinates, but separated by a given distance along the  $y$ -direction. Then, an average is taken for all the possible  $(x, z)$  locations. Due to periodic boundary conditions only five out of the ten unit cells along  $y$  in our supercell are relevant and bring new information.

The system also presents a strong anisotropy between the  $x$  and  $z$  directions, due to the fact that along  $z$  the  $\text{PbTiO}_3$  layers are sandwiched in between dielectric  $\text{SrTiO}_3$  layers. The  $z$ -component of the polarization within the  $\text{PbTiO}_3$  layers breaks down into domains to minimize the depolarizing fields. On the other hand, along the  $x$ -direction we find an homogeneous periodically repeated media: a  $\text{PbTiO}_3$  layer without electrostatic constrains. Due to this fact we have a difficulty to study the correlations in the  $xz$ -plane, since making a displacement  $\mathbf{R}$  to compute the correlation function along the  $x$  or  $z$  directions is not equivalent. To solve this problem, instead of studying the correlation as a function of the distance  $|\mathbf{R}|$  in the  $xz$ -plane, similar to the analysis carried out before, we have decided to study both components separately.

The obtained results suggest the existence of three different phases that can be distinguished by both their polarization patterns and symmetry aspects, and by their correla-

tion functions. In the following we shall be addressing the outcomes of the temperature evolution study of the system.

Clearly, the vortices represented in Fig. 26 do not hold the premises required to apply the Mermin-Wagner theorem (dimensionality, long range interactions, strong anisotropies,...). Therefore this theorem cannot be applied and we would expect to have a broken symmetry phase with certain order at finite temperatures. In fact this is what it occurs and the phase presented in Fig. 26 is stable up to  $T = 70$  K. In Fig. 28 we address the results of the correlation function along the  $x$  direction for some temperatures within this range. There we can see what is evidenced by Fig. 26, the existence of an order determined by the  $p_z > 0$  and  $p_z < 0$  domains that appear in between the vortex textures.

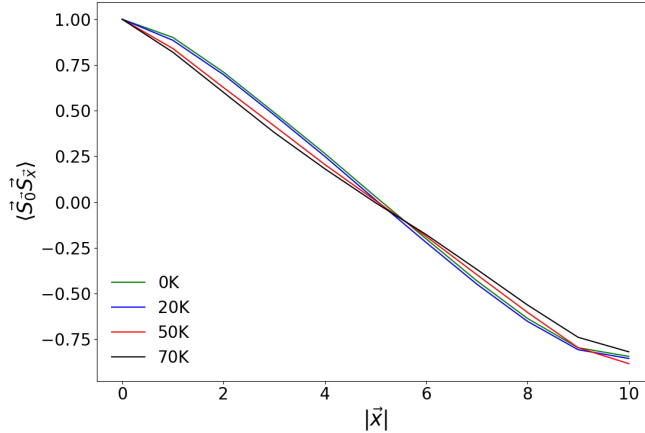


Figure 28: Correlation function for dipoles with the same  $(y, z)$  location, as a function of the number of unit cells that separates them along the  $x$  direction in the low-temperature phase. Colors represent different temperatures as specified in the legend.

These results evidence the presence of ferroelectric domains of about ten unit cells width, like the ones presented in Fig. 26. The correlations are constant for every plane, independently of the distance between them along the  $y$ -direction (see Fig. 27). In fact if we plot the polarization pattern we would not find remarkable differences with respect to the one presented above in Fig. 26. We are thus still in the same ordered phase, even if we are already at finite temperatures.

The first transition that we observe is present for higher temperatures, in between 70 K and 80 K, and is related with the mobility of the domain wall. In this intermediate temperature phase if we focus on a given  $y$  plane it is characterized by the widening of one domain with respect to the other as it is shown in Fig. 29 (a). This translates into

a change in the correlation function as we no longer have equal-sized even domains for a given  $y$  plane. However the overall polarization within the supercell averages to zero, which means that for other  $y$  planes the opposite happens, as shown in Fig. 29 (b). This can be understood as a plastic domain wall that moves as we change the  $y$  coordinate of the supercell. This difference of the polarization pattern for different  $y$  planes translates into a decay of the correlation function along the  $y$  direction with respect to the curve obtained in the previous low-temperature phase, as illustrated in Fig. 30

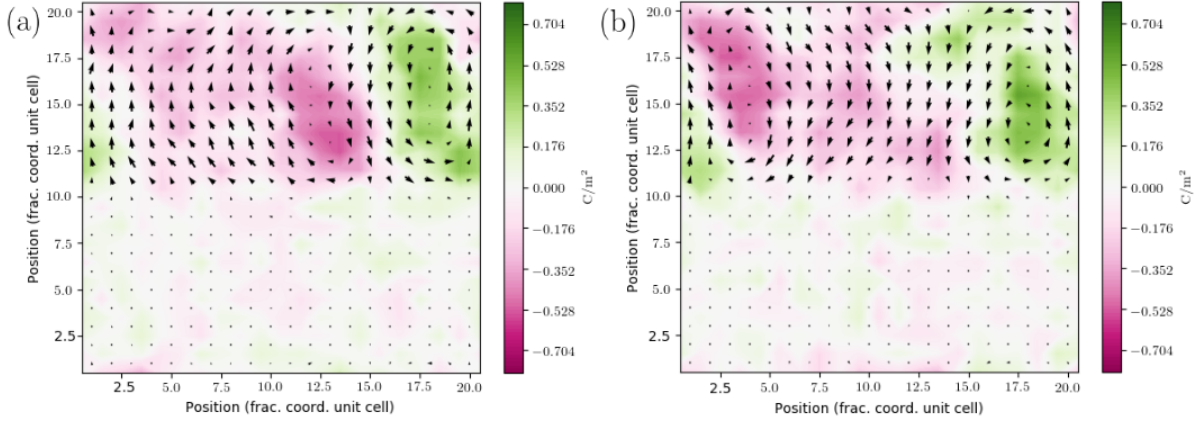


Figure 29: Two different planar sections of the polarization pattern, corresponding to different values of  $y$  at  $T = 80$  K. It is clearly shown how in (a) there is a dominance of the  $p_z > 0$  domain, whereas in (b) the opposite occurs. In average the polarization vanishes in the supercell.

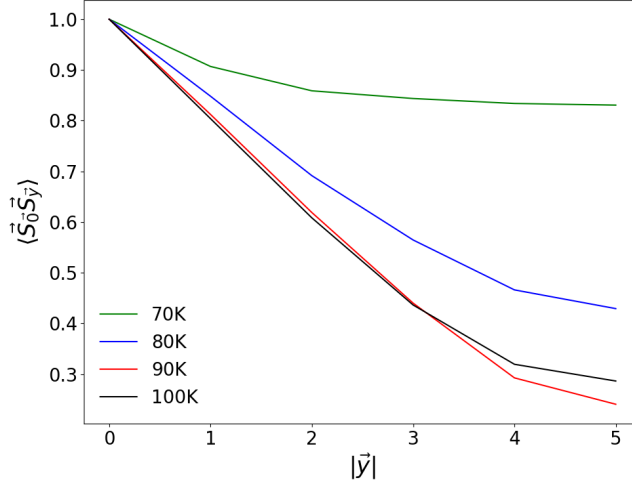


Figure 30: Correlation function along the  $y$  direction as a function of the temperature where we can distinguish two different behaviours. In the low temperature phase (represented by the 70 K green curve) the correlation remains high even for large distances, whereas in the intermediate temperature phase (represented by the 80, 90, and 100 K curves) the correlation decays as a function of the distance along the  $y$ -direction.

This appreciable change in the plane by plane polarization pattern is of course accompanied by a large difference in the behaviour of the  $x$ -correlation function that is addressed below. Due to the fact that the up and down domains are not equal sized in a given  $y$ -plane, our correlation function does not reach negative values close to -1 for a distance of the width of the domain, as it happened in Fig. 28 or in the toy model of Fig. 10(b). This intermediate phase extends up to the complete melting of the domain wall which is observed in between 190–200 K. All along the temperature range between 100 and 190 K, the dipole pattern presents qualitatively the same behaviour and the correlation functions are similar, except on the faster decay induced by the raise of temperature disorder and some aspects derived from the fact that the widening of the domain is more accused when the temperature is increased.

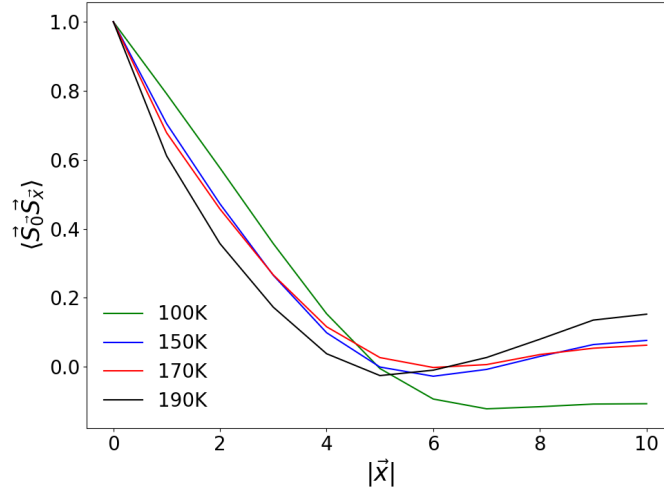


Figure 31: Correlation function for dipoles with the same  $(y, z)$  location, as a function of the number of unit cells that separates them along the  $x$  direction in the intermediate temperature phase. Colors represent different temperatures as specified in the legend.

The last phase that we have observed in our simulations comes from the melting of the domain wall at high-enough temperature, and is characterized by a complete disorder of the dipole pattern as it is shown in Fig. 32, with the concomitant correlation functions presenting exponential decays (Fig. 33).

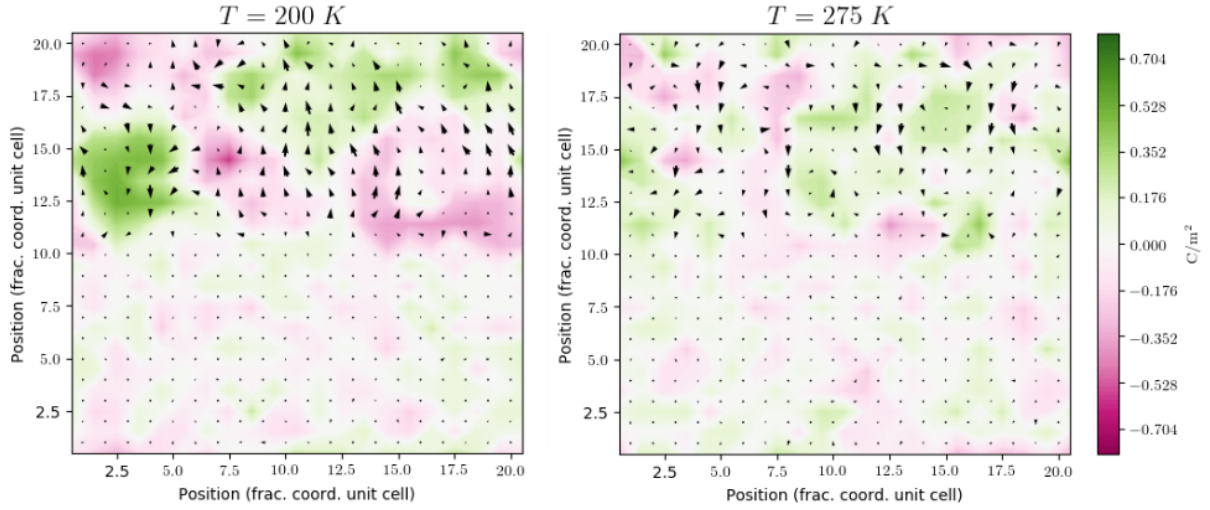


Figure 32: Section of the dipole pattern adopted by the system in the high temperature phase at two different temperatures. The domain wall is absent and a disordered state is observed.

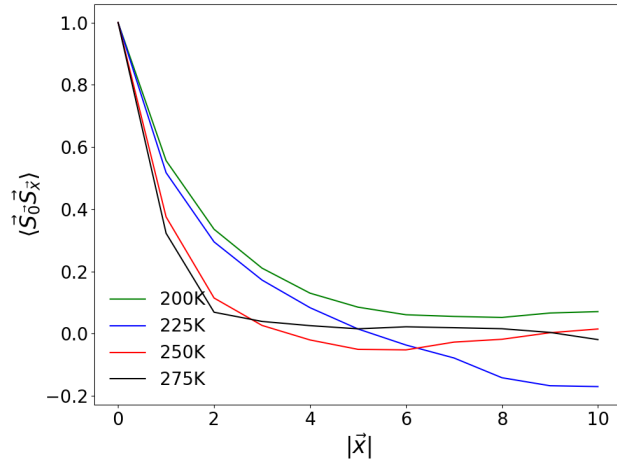


Figure 33: Correlation function for dipoles with the same  $(y, z)$  location, as a function of the number of unit cells that separates them along the  $x$  direction in the high temperature phase. Colors represent different temperatures as specified in the legend.

The analysis of the data is not as straight forward as it was in the previous model. The functional forms to fit the data must be modified to proceed with the proper interpretation

of the results. In particular, the  $x$ -correlation of the low temperature phase is easy to analyze, as we only have alternating up and down domains and we can fit the data to a cosine type function from which we can extract the width of the domains. From the simplified discussion carried out in Fig. 10, in the toy models we used at the time of defining the correlation function, we would expect that ferroelectric domains should display a straight line. Here, as shown in Fig. 34, this is not the case, since the presence of vortex textures produce a certain canting near the vortex that induce a spin-wave like cosine behaviour.

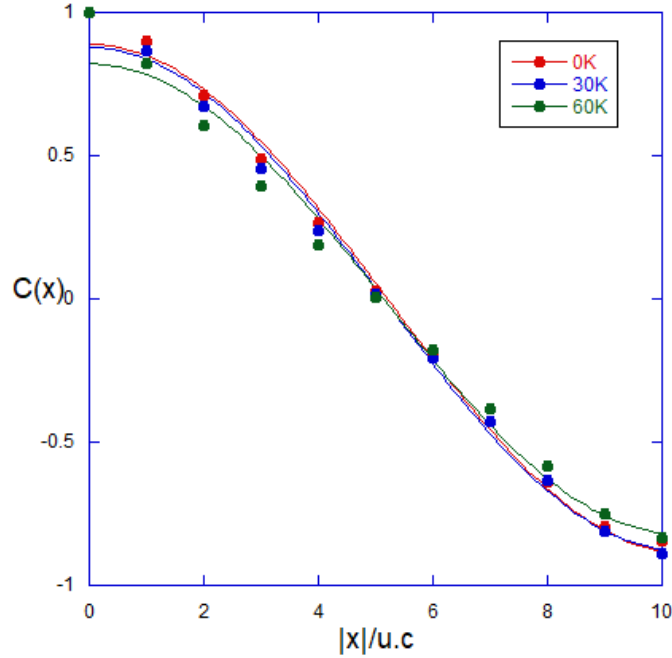


Figure 34: Correlation function for dipoles as a function of the number of unit cells that separates them along the  $x$  direction. Colors represent different temperatures as specified in the legend. Solid lines correspond to fits to the functional form  $C(x) = a_0 \cdot \cos\left(\frac{\pi x}{a_1}\right)$

From the period of the cosine functions we can extract the width of the domains, that for all the tested temperatures amounts to values around  $10.3 \pm 0.2$  u.c., matching the nominal value of 10 unit cells for the domain widths considered in the simulation box. This phase corresponds to the long-ordered low-temperature phase that we also encountered in the previous model of Sec. 8.1.

Although the mobility of the domain wall is expected to occur, we might wonder if we could detect any hint of BKT-like behaviour superimposed to the fall of the correlation

due to this fact. In order to treat the intermediate temperature phase, we noticed that two different physical mechanisms are taking place. On the one hand, we now have a mobile domain wall that produces the widening of one domain at the expenses of the other. On the other hand we find a certain thermal disorder inside each of the domains. As a consequence, and assuming that both effects are independent, we decided to fit the data to a product of cosines (that explains the fall of the correlation function due to the presence of different domain sizes) and a decaying function (that explains the disorder within each of the domains). For the functional form of the decaying function we tried with power-law like decay and exponential like decay resulting in the two following types of functional forms

$$C_1(x) = \cos(a_0 \cdot x) \cdot \cos(a_1 \cdot x) \cdot (x + 1)^{-\eta}, \quad (43)$$

$$C_2(x) = \cos(a_0 \cdot x) \cdot \cos(a_1 \cdot x) \cdot e^{-\frac{x}{\xi}}. \quad (44)$$

Our results show that there exists a small temperature window in between  $80 \sim 90$  K where the power-law decay fits better the disorder within the domains than the exponential one. Interestingly this phase emerges when the coupling between the different  $y$  planes decreases as a consequence of the plastic domain wall, hence producing the appearance of an “effective” two-dimensional system as it happened in Ref. (25).

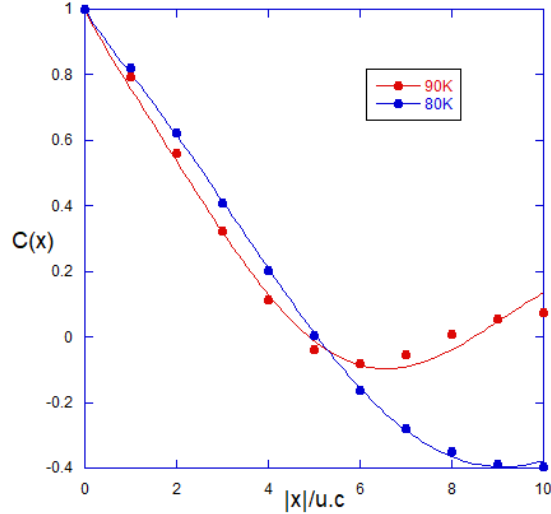


Figure 35: Correlation function for dipoles as a function of the number of unit cells that separates them along the  $x$  direction. Colors represent different temperatures as specified in the legend. Solid lines correspond to fits to the functional form  $C_1(x)$  given in Eq. (43)

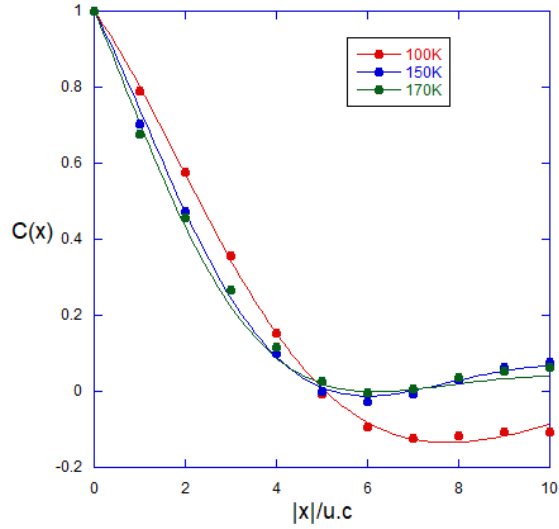


Figure 36: Correlation function for dipoles as a function of the number of unit cells that separates them along the  $x$  direction. Colors represent different temperatures as specified in the legend. Solid lines correspond to fits to the functional form  $C_2$  given in Eq. (44)

What we obtain is that in fact the domains are wider, of about 14 to 17 u.c., but that the type of disorder within each domain changes from a QLRO (in between 80-90 K) to a disordered behaviour (for higher temperatures).

Finally, the high temperature phase once the domain wall has melted the only contribution that remains is the exponential decay due to thermal fluctuations and that characterizes the disordered phase.

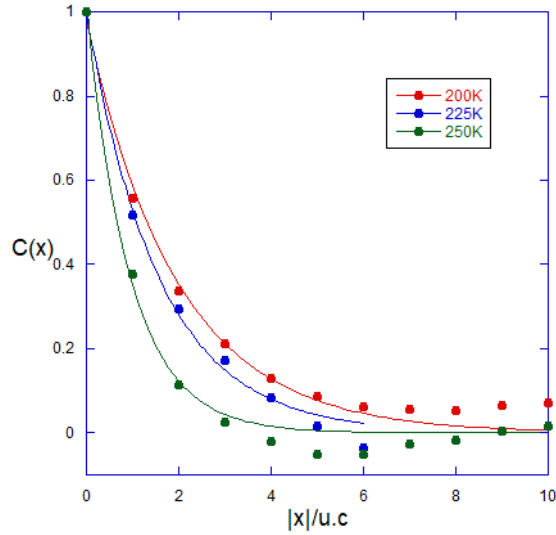


Figure 37: Correlation function for dipoles as a function of the number of unit cells that separates them along the  $x$  direction. Colors represent different temperatures as specified in the legend. Solid lines correspond to fits to the functional form  $a_0 \cdot e^{-\frac{x}{a_1}}$

What we can obtain from the fits of Fig. 35-Fig. 37 is that the critical exponents found in the fitting where  $\eta = 0.240 \pm 0.011$  for  $T = 80$  K and  $\eta = 0.29 \pm 0.04$  for  $T = 90$  K which reminds us to the theoretical predicted value of  $\frac{1}{4}$  studied in Sec. 6.1 near the transition. Moreover, the evolution of the correlation length with temperature are collected in Table 2.

$T/K$	$\xi/u.c$
100	$6.0 \pm 0.3$
110	$5.7 \pm 0.3$
120	$5.6 \pm 0.3$
130	$5.0 \pm 0.3$
150	$4.4 \pm 0.2$
170	$3.5 \pm 0.3$
200	$1.96 \pm 0.13$
225	$1.57 \pm 0.09$
250	$0.95 \pm 0.07$

Table 2: Results obtained for the correlation length as a function of temperature obtained from the fits in Fig. 36 and Fig. 37.

Although the temperature sampling is not fine enough (we have only explored two tem-

peratures in the interesting range between  $80 \sim 90$  K), our results are promising with respect the existence of BKT transitions in  $\text{PbTiO}_3/\text{SrTiO}_3$  superlattices with alternating clockwise/counter-clock-wise vortices. Although not totally conclusive (a more detailed statistic is required) we observe hints on how there is a window of temperatures where the disorder within each of the domains is explained by a power-law decay which would result in the observation of BKT-like transitions in a three dimensional model with a three dimensional order parameter. Very interestingly the QLRO phase appear when the coupling between planes decreases, and hence induces in the system a certain two-dimensional behaviour. More simulations are needed to capture the evolution of the correlation length with temperature, expected to present an exponential divergence near the transition temperature, as observed by Ghosh *et al.* in Ref. (27).

## 9 Conclusions

During this work we have studied in depth the classical XY-model, deriving its behaviour at low- and high- temperature limits and observing the celebrated Berezinskii–Kosterlitz–Thouless phase transitions. Afterwards, we have gone through all the critical assumptions within the model trying to extract their relevance and revising in the existing bibliography whether they are crucial or not to observe these type of phenomena. Finally, after applying all the theory developed in the work to the case of  $\text{PbTiO}_3/\text{SrTiO}_3$  superlattices we can highlight the following main points.

1. The presence of an ordered phase at finite temperatures does not prevent the existence of a phase transition carried by pattern formation mediating between the ordered and disordered phases. In the XY-model where Mermin-Wagner theorem applies this is the unique possible type of transition however, in other systems first- or second- order phase transitions may coexist with BKT.
2. The effect of long range interactions does not mandatorily exclude the existence of topological defects. Although long range interactions tend to stabilize fluctuations, what usually happens is that topological defects become relevant at higher temperatures.
3. The topological characterization of a given pattern depends much on the topology of the order parameter space. However, the fact that a defect is not topologically stable in a system does not prohibit it existence as it can be thermodynamically favoured.
4. BKT transitions are present in two-dimensional ferroelectrics (26).
5. BKT transitions are also present in low-dimensional systems constituted by thin films of ferroelectric materials(25).

6. We could detect BKT behaviour in the  $\text{PbTiO}_3/\text{SrTiO}_3$  superlattice model when the polarization was confined to the  $xy$ -plane.
7. We could detect some hints that BKT behaviour might also be possible in the second model treated in the work. Further investigation is under development within this model.
8. The physics of the system depends on the elastic boundary conditions inducing completely different behaviours and interactions that make possible the existence of BKT in 3D even if this is not possible in classical 3D planar or Heisenberg models.
9. Even when treating 3D systems the QLRO phases seems to appear when the coupling between the different section planes under consideration is low reminding us to a “effectively” 2D system.

## References

- [1] N. D. Mermin and H. Wagner. Absence of ferromagnetism or antiferromagnetism in one- or two-dimensional isotropic Heisenberg models. *Phys. Rev. Lett.*, 17:1133–1136, Nov 1966. URL: <https://link.aps.org/doi/10.1103/PhysRevLett.17.1133>, doi:10.1103/PhysRevLett.17.1133.
- [2] J M Kosterlitz and D J Thouless. Long range order and metastability in two dimensional solids and superfluids. (Application of dislocation theory). *Journal of Physics C: Solid State Physics*, 5(11):L124–L126, jun 1972. URL: <https://doi.org/10.1088%2F0022-3719%2F5%2F11%2F002>, doi:10.1088/0022-3719/5/11/002.
- [3] J M Kosterlitz and D J Thouless. Ordering, metastability and phase transitions in two-dimensional systems. *Journal of Physics C: Solid State Physics*, 6(7):1181–1203, apr 1973. URL: <https://doi.org/10.1088%2F0022-3719%2F6%2F7%2F010>, doi:10.1088/0022-3719/6/7/010.
- [4] The Royal Swedish Academy of Science. Topological phase transition and topological phases of matter. <https://www.nobelprize.org/uploads/2018/06/advanced-physicsprize2016.pdf>. Access 11-06-2020.
- [5] V. L. Berezinskii. Destruction of long-range order in one-dimensional and two-dimensional systems having a continuous symmetry group I. Classical systems. *Soviet Journal of Experimental and Theoretical Physics*, 32(3):493–500, 1971.
- [6] V. L. Berezinskii. Destruction of long-range order in one-dimensional and two-dimensional systems possessing a continuous symmetry group. II. Quantum Systems. *Soviet Journal of Experimental and Theoretical Physics*, 34(3):610–616, 1972.

- [7] M. V. Fistul, V. M. Vinokur, and T. I. Baturina. Collective cooper-pair transport in the insulating state of Josephson-Junction Arrays. *Phys. Rev. Lett.*, 100:086805, Feb 2008. URL: <https://link.aps.org/doi/10.1103/PhysRevLett.100.086805>, doi:10.1103/PhysRevLett.100.086805.
- [8] Luca Capriotti, Alessandro Cuccoli, Andrea Fubini, Valerio Tognetti, and Ruggero Vaia. Berezinskii-Kosterlitz-Thouless transition in Josephson Junction Arrays. *Fundamental Problems of Mesoscopic Physics*, page 203–216. URL: [http://dx.doi.org/10.1007/1-4020-2193-3\\_12](http://dx.doi.org/10.1007/1-4020-2193-3_12), doi:10.1007/1-4020-2193-3\_12.
- [9] G. Blatter, M. V. Feigel'man, V. B. Geshkenbein, A. I. Larkin, and V. M. Vinokur. Vortices in high-temperature superconductors. *Rev. Mod. Phys.*, 66:1125–1388, Oct 1994. URL: <https://link.aps.org/doi/10.1103/RevModPhys.66.1125>, doi:10.1103/RevModPhys.66.1125.
- [10] David R. Nelson. Vortex entanglement in high- $T_c$  superconductors. *Phys. Rev. Lett.*, 60:1973–1976, May 1988. URL: <https://link.aps.org/doi/10.1103/PhysRevLett.60.1973>, doi:10.1103/PhysRevLett.60.1973.
- [11] P. M. Chaikin and T. C. Lubensky. *Principles of Condensed Matter Physics*. Cambridge University Press, Cambridge, 1995.
- [12] M. Kardar. *Statistical Physics of Fields*. Cambridge University Press, 2007. doi:10.1017/CB09780511815881.
- [13] M. Carmen Miguel. Notes: IX GEFENOL summer school on statistical physics of complex systems.
- [14] A. Cheung. Phase transitions and collective phenomena. <https://www.tcm.phy.cam.ac.uk/~achc2/phase/notes.pdf>. Access 03-02-2020.
- [15] J M Kosterlitz. The critical properties of the two-dimensional xy model. *Journal of Physics C: Solid State Physics*, 7(6):1046–1060, mar 1974. URL: <https://doi.org/10.1088%2F0022-3719%2F7%2F6%2F005>, doi:10.1088/0022-3719/7/6/005.
- [16] P. G. Maier and F. Schwabl. Ferromagnetic ordering in the two-dimensional dipolar xy model. *Phys. Rev. B*, 70:134430, Oct 2004. URL: <https://link.aps.org/doi/10.1103/PhysRevB.70.134430>, doi:10.1103/PhysRevB.70.134430.
- [17] A. Yu Vasiliev, A. E. Tarkhov, L. I. Menshikov, P. O. Fedichev, and Uwe R. Fischer. Universality of the Berezinskii–Kosterlitz–Thouless type of phase transition in the dipolar XY-model. *New Journal of Physics*, 16(5):053011, may 2014. URL: <https://doi.org/10.1088%2F1367-2630%2F16%2F5%2F053011>, doi:10.1088/1367-2630/16/5/053011.

- [18] P. O. Fedichev and L. I. Men'shikov. BKT phase transition in a 2D system with long-range dipole-dipole interaction. *Physics of Particles and Nuclei Letters*, 9(1):71–75, Jan 2012. URL: <https://doi.org/10.1134/S1547477112010098>, doi:10.1134/S1547477112010098.
- [19] P.G. Maier and F. Schwabl. Novel phase transition in two-dimensional xy-models with long-range interaction. *Condensed Matter Physics*, 8:103–111, 2005. doi:10.5488/CMP.8.1.103.
- [20] G. Ortiz, E. Cobanera, and Z. Nussinov. Dualities and the phase diagram of the p-clock model. *Nuclear Physics B*, 854(3):780 – 814, 2012. URL: <http://www.sciencedirect.com/science/article/pii/S0550321311005219>, doi:<https://doi.org/10.1016/j.nuclphysb.2011.09.012>.
- [21] J.R. Munkres. *Topology*. Featured Titles for Topology. Prentice Hall, Incorporated, 2000. URL: <https://books.google.es/books?id=XjoZAQAIAAJ>.
- [22] Naoto Nagaosa and Yoshinori Tokura. Topological properties and dynamics of magnetic skyrmions. *Nature Nanotechnology*, 8(12):899–911, Dec 2013. URL: <https://doi.org/10.1038/nnano.2013.243>, doi:10.1038/nnano.2013.243.
- [23] I. Herbut. *A Modern Approach to Critical Phenomena*. Cambridge University Press, 2007.
- [24] S. Ahamed, S. Cooper, V. Pathak, and W. Reeves. The Berezinskii-Kosterlitz-Thouless transition. <https://www.phas.ubc.ca/~berciu/TEACHING/PHYS502/PROJECTS/18BKT.pdf>. Access 15-06-2020.
- [25] Y. Nahas, S. Prokhorenko, I. Kornev, and L. Bellaiche. Emergent Berezinskii-Kosterlitz-Thouless phase in low-dimensional ferroelectrics. *Phys. Rev. Lett.*, 119:117601, Sep 2017. URL: <https://link.aps.org/doi/10.1103/PhysRevLett.119.117601>, doi:10.1103/PhysRevLett.119.117601.
- [26] C. Xu, Y. Nahas, S. Prokhorenko, H. Xiang, and L. Bellaiche. Berezinskii-Kosterlitz-Thouless phase in two-dimensional ferroelectrics. *Phys. Rev. B*, 101:241402, Jun 2020. URL: <https://link.aps.org/doi/10.1103/PhysRevB.101.241402>, doi:10.1103/PhysRevB.101.241402.
- [27] A. Ghosh, S. Das, V. Stoica, F. Gómez-Ortiz, M. R. McCarter, C. Dai, H. Wen, D. Walko, G. Velarde, C. Nelson, V. Gopalan, D.-H. Lee, J. Freeland, P. García-Fernández, J. Junquera, L.-Q. Chen, E. Dufresne, R. Ramesh, and L. W. Martin. Topological-phase transition and protection in ferroelectric vortices. submitted to *Nature Materials*, 2020.

- [28] P. Shafer, P. García-Fernández, P. Aguado-Puente, A. R. Damodaran, A. K. Yadav, C. T. Nelson, Shang-Lin Hsu, J. C. Wojdeł, J. Íñiguez, L. W. Martin, E. Arenholz, J. Junquera, and R. Ramesh. Emergent chirality in the electric polarization texture of titanate superlattices. *Proc. Natl. Acad. Sci. U.S.A.*, 115(5):915–920, 2018. URL: <https://www.pnas.org/content/115/5/915>, doi:10.1073/pnas.1711652115.
- [29] J. C. Wojdeł, P. Hermet, M. P. Ljungberg, P. Ghosez, and J. Íñiguez. First-principles model potentials for lattice-dynamical studies: general methodology and example of application to ferroic perovskite oxides. *Journal of Physics: Condensed Matter*, 25(30):305401, jul 2013. URL: <https://doi.org/10.1088/0953-8984/25/30/305401>, doi:10.1088/0953-8984/25/30/305401.
- [30] A. K. Yadav, C. T. Nelson, S. L. Hsu, Z. Hong, J. D. Clarkson, C. M. Schlepütz, A. R. Damodaran, P. Shafer, E. Arenholz, L. R. Dedon, D. Chen, A. Vishwanath, A. M. Minor, L. Q. Chen, J. F. Scott, L. W. Martin, and R. Ramesh. Observation of polar vortices in oxide superlattices. *Nature*, 530(7589):198–201, 2016. URL: <https://doi.org/10.1038/nature16463>, doi:10.1038/nature16463.
- [31] G. Arfken. *Mathematical Methods for Physicists*. Academic Press, Inc., San Diego, third edition, 1985.
- [32] D. Packard. Introduction to the Berezinskii-Kosterlitz-Thouless transition. [http://guava.physics.uiuc.edu/~nigel/courses/563/Essays\\_2013/PDF/Packard.pdf](http://guava.physics.uiuc.edu/~nigel/courses/563/Essays_2013/PDF/Packard.pdf), 2013. Access 08-03-2020.
- [33] P. García-Fernández, J. C. Wojdeł, J. Íñiguez, and J. Junquera. Second-principles method for materials simulations including electron and lattice degrees of freedom. *Phys. Rev. B*, 93:195137, May 2016. URL: <https://link.aps.org/doi/10.1103/PhysRevB.93.195137>, doi:10.1103/PhysRevB.93.195137.

## A Energy of different spin textures.

In this appendix we shall try to give some insight and develop an intuitive idea of why the energy of an isolated vortex presents a quadratic dependence on the vorticity of the spin texture.

First, as we would expect, we shall prove that a vortex and an anti-vortex presents the same energy. This is sensible since the only difference between them is that the sense of rotation is opposite although its modulus is the same. The field

$$\theta = \arctan\left(\frac{x}{y}\right),$$

reproduces an anti-vortex like the one shown in the Fig. 38.

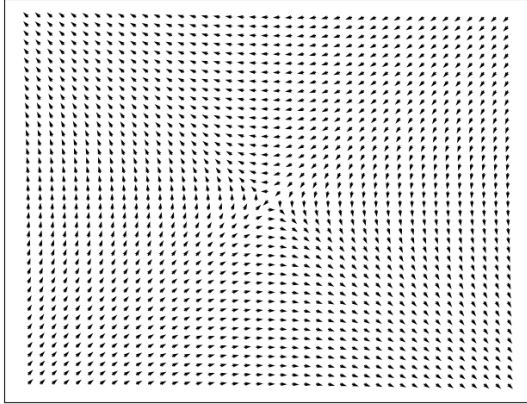


Figure 38: Example of an anti-vortex spin texture.

Doing the same exercise that we did in the main text we can compute  $|\nabla\theta|^2 = \frac{x^2+y^2}{(x^2+y^2)^2}$  that presents exactly the same form as the source spin texture shown in Fig. 4 and hence gives the same energy.

As a last example we shall study now a spin texture of vorticity  $n = 2$ , the dipole field, that has an analytical expression of  $\theta = \arctan\left(\frac{x^2-y^2}{-2xy}\right)$  and presents the texture shown in Fig. 39.

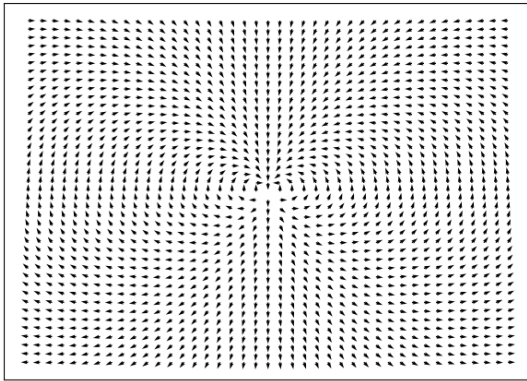


Figure 39: Example of a dipole spin texture.

As the reader can confirm this field presents vorticity  $n = 2$  at the origin and after some basic derivatives one can find that  $|\nabla\theta|^2 = 4 \cdot \frac{x^2+y^2}{(x^2+y^2)^2}$  and hence the energy of a dipole pattern has  $n^2 = 4$  times more energy than the normal vortex studied in the main text.

Finally we shall try to give an intuitive idea of why this is happening. If we remember our boundary conditions stated in Eq. (8) and assume that the variation of  $\theta$  is constant along the circulation, we have that

$$2\pi n = \oint \nabla\theta(\mathbf{r})d\mathbf{l} = 2\pi r|\nabla\theta|,$$

hence  $|\nabla\theta|^2 = \frac{n^2}{r^2}$ , and when we integrate in polar coordinates we recover the quadratic dependence of Eq. (12), as confirmed by the expressions above.

If the reader is used to algebraic topology he/she can notice that this continuous deformation can always be done in order to transform the texture and make the distortion uniform along the circulation path. All the examples of fields taken into account in this text presented this characteristic. Of course this continuous deformation may alter the energy of the physical system. But we can differentiate between the topological part of the energy presenting the quadratic dependence with the vorticity, and a physical part independent of the vorticity that accounts for the particular (not uniform) tilting that the original texture might present.

## B Resolution of singularities via renormalization.

In this Appendix we shall focus on proving Eq. (14). This is a consequence of a well-known theorem of algebraic topology (summarized in Fig. 40) which states that our loop can be decomposed as the concatenation of several loops that enclose each of the singularities independently.

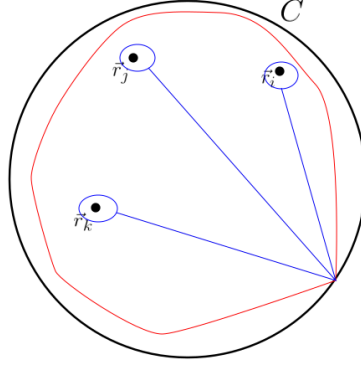


Figure 40: Consecutive continuous transformations of our loop  $C$  in black, red and blue loops, where we show how our original loop  $C$  is homotopic to the concatenation of the loops that enclose individually each of the singularities and so  $\iint_{int C} \nabla \times \nabla \theta = \sum_i \iint_{int C_i} \nabla \times \nabla \theta$ .

This allows us to locate the topological charge at specific discrete points in the space (remember that the singularities of our field were isolated) and hence rewrite our field as a sum of (i) a non-singular part  $\theta_0$  (a continuous function with all its derivatives continuous, or  $\mathcal{C}^\infty$  function); and (ii) a distribution that accumulates all the non-trivial topological aspects of our field,

$$\nabla \theta = \nabla \theta_0 - \nabla \times \hat{e}_z \psi, \quad (45)$$

where  $\psi$  is a still unknown scalar field that will account for the topological part. Since the first term in the right-hand side is rotational free, we have that

$$\nabla \times \nabla \theta = -\nabla \times \nabla \times \hat{e}_z \psi = \hat{e}_z \nabla^2 \psi. \quad (46)$$

In order to arrive to this conclusion, we have applied Eq. (1.80) of Ref. (31)

$$\nabla \times (\nabla \times \vec{V}) = \nabla (\nabla \cdot \vec{V}) - \nabla \cdot \nabla \vec{V}, \quad (47)$$

and

$$\begin{aligned} \nabla \cdot \nabla \vec{V} &= \hat{i} \nabla \cdot \nabla V_x + \hat{j} \nabla \cdot \nabla V_y + \hat{k} \nabla \cdot \nabla V_z \\ &= \hat{i} \nabla^2 V_x + \hat{j} \nabla^2 V_y + \hat{k} \nabla^2 V_z. \end{aligned} \quad (48)$$

If we consider  $\vec{V} = \hat{e}_z \psi$  in Eqs. (47)-(48), and taking into account that any derivative of  $\psi$  with respect to  $z$  is zero since we are working only in the  $(x, y)$  plane, we recover the expression in Eq. (46).

Gathering together Eq. (14) and Eq. (46), we arrive to the following Poisson-like equation

$$\nabla^2\psi = 2\pi \sum_i n_i \delta^2(\mathbf{r} - \mathbf{r}_i). \quad (49)$$

## C Derivation of the energy of interacting singularities

In this appendix we develop the derivation in order to obtain the interaction energy between vortices. Similar approaches can be found in (12; 3; 32). As it is said in the main text in order to do so we have to integrate:

$$\begin{aligned} \mathcal{H} &= \frac{J}{2} \iint dxdy |\nabla\theta(x, y)|^2 \\ &= \frac{J}{2} \iint dxdy [(\nabla\theta_0)^2 - 2\nabla\theta_0 \cdot \nabla \times \hat{e}_z\psi + (\nabla \times \hat{e}_z\psi)^2]. \end{aligned}$$

We can neglect the second term of the right-hand side of the equation if we integrate it by parts

$$\iint_{\Omega} 2\nabla\theta_0 \cdot \nabla \times \hat{e}_z\psi dxdy = \int_{\partial\Omega} \theta_0 n(x) d\sigma(x) - \iint_{\Omega} \nabla(\nabla \times \hat{e}_z\psi) \theta_0$$

as the divergence of a curl is zero and assuming no boundary conditions for the auxiliary field  $\theta_0$  this can always be considered by continuously deform the field.

The last term can be simplified by noting that

$$\nabla \times \hat{e}_z\psi = \begin{vmatrix} \hat{e}_x & \hat{e}_y & \hat{e}_z \\ \partial_x & \partial_y & \partial_z \\ 0 & 0 & \psi \end{vmatrix} = \hat{e}_x \partial_y \psi - \hat{e}_y \partial_x \psi,$$

and, therefore,  $(\nabla \times \hat{e}_z\psi)^2 = (\partial_y\psi)^2 + (\partial_x\psi)^2 = (\nabla\psi)^2$ . Again, we have considered that any derivative with respect to  $z$  vanishes. Integrating this term by parts we end up with the following expression for the topological part of the Hamiltonian

$$\mathcal{H}_{top} = \frac{J}{2} \oint_{\partial\Omega} \psi n(x) d\sigma(x) - \frac{J}{2} \iint dxdy \psi \nabla^2\psi, \quad (50)$$

where the form of the Laplacian is given by Eq. (49). In order to get an analytical form for  $\psi$  we have to solve that Poisson equation in two dimensions.

Hence we can see that  $\psi$  will present the form of a potential generated by punctual charges located at positions  $\mathbf{r}_i$ . Following Eq. (16.157) of Arken's book (31), if

$$\nabla^2 G(\mathbf{r}_1, \mathbf{r}_2) = -\delta(\mathbf{r}_1 - \mathbf{r}_2), \quad (51)$$

then an integration in two-dimensional space gives [Eq. (16.161) of Ref. (31)]

$$G(\mathbf{r}_1, \mathbf{r}_2) = -\frac{1}{2\pi} \ln(|\mathbf{r}_1 - \mathbf{r}_2|). \quad (52)$$

Particularizing Eq. (52) to our problem, then  $\psi$  is the Green function for two dimensions and has the following form

$$\psi = \sum_i n_i \ln(|\mathbf{r} - \mathbf{r}_i|) + cte. \quad (53)$$

Plugging this form of both  $\psi$  and  $\nabla^2\psi$  into Eq. (50) we realize that the first term scales as  $\ln(L) \left(\sum_i n_i\right)^2$  (see Chapter 8.2 of (12)) since integrating on a region that encloses all the singularities present the same disturbance from a large scale perspective that a single vortex of vorticity  $\sum_i n_i$  as the ones studied in Appendix A. Therefore in the thermodynamic limit only neutral configurations  $\sum_i n_i = 0$  are energetically affordable. The second term remains and the energy of the interaction is

$$\mathcal{H}_{top} = -\frac{J}{2} \iint dx dy \left( \sum_i \sum_j n_i \ln(|\mathbf{r} - \mathbf{r}_i|) + cte \right) \cdot 2\pi n_j \delta^2(\mathbf{r} - \mathbf{r}_j), \quad (54)$$

and therefore the energy of the system presents the following form.

$$E = -\frac{J}{2} \sum_i \sum_j 2\pi n_i n_j (\ln(|\mathbf{r}_i - \mathbf{r}_j|) + cte). \quad (55)$$

As we can see we have a divergence for the terms where our “potential” is singular (i.e. where  $\mathbf{r}_i = \mathbf{r}_j$ ). We can split this divergence in two terms as follows and therefore the energy of the system presents the following form in accordance with (12).

$$E = -J \cdot V(0) \pi \left( \sum_i n_i \right)^2 - \frac{J}{2} \sum_i \sum_{j \neq i} 2\pi n_i n_j (\ln(|\mathbf{r}_i - \mathbf{r}_j|) + cte), \quad (56)$$

where  $V(0)$  represents the divergence of the self interaction energy. This divergent term can be neglected since as we have proven only neutral configurations are affordable. However, this can be shown again by noting that the first term leads to a zero contribution to the partition function provided that the weight of each distribution is related with  $e^{-\beta E}$ . As  $V(0) = \ln(0) \rightarrow -\infty$  we would have that the weight of such a distribution is  $e^{\frac{-1}{k_B T} (\sum_i n_i)^2 \cdot \infty}$  which is zero unless we have a zero net charge  $\sum_i n_i = 0$  as we expected.

This fact means that only neutral configurations are allowed or, which is the same, vortex

and anti-vortex should be compensated. Now that we have this information we can find a simpler expression for Eq. (56) by using the relation

$$0 = \left( \sum_i n_i \right)^2 = \sum_i n_i^2 + 2 \sum_i \sum_{i \neq j} n_i n_j.$$

This leads to the expression used in the main text.

## D Computational aspects.

The computational technique used in the study of this work are as mentioned in the main text second principles density functional theory (SPDFT) together with Monte Carlo sampling. Second principles methods are born to solve some of the main problems within first principles ones applied to solids allowing hence for example the study of large-scale systems (10-100 nm) composed of big supercells or making possible the study of non-stationary systems that evolve in time (hundreds of ps) even under temperature conditions. Therefore second principles allow us to build models capable of treating such interesting and complex problems with an accuracy limited by DFT, these methods are implemented in Scale-Up code. The size of the system under study during this work as well as the temperature sampling in which we are interested in make essential the use of these techniques.

The fundamental idea behind second principles methodology is dividing the electronic density as a reference density ( $n_0$ ) and a perturbation ( $\delta n$ ). Typically the reference density represents the electronic density of the ground state and is a parameter in the model which reduces the number of calculations

$$n(\vec{r}) = n_0(\vec{r}) + \delta n(\vec{r}). \quad (57)$$

With this approach we can obtain the energy of an excited state by making a perturbative expansion of the functional of the energy typically truncated at second order

$$E_{DFT} \approx E^{(0)} + E^{(1)} + E^{(2)} + \dots \quad (58)$$

The first term  $E^{(0)}$  corresponds to what is called the electron-lattice term if we assume no deviation from the reference geometry this term corresponds to the DFT energy of the reference structure (as we mentioned earlier usually the ground state of the system in its equilibrium geometry) and depends only on  $n_0$ . This term is the one that we are interested in in this work since we shall be sampling different geometrical distortions of the unit cell in such a way that we can explore all possible polarization profiles. As any displacements of the atoms can be related with polarization via born effective charges

$$P = \sum_{i \in atoms} Z_i^* \delta x_i,$$

where  $Z_i^*$  represent the Born effective charge of the given atom and  $\delta x_i$  its displacement with respect to the reference geometry. This coupling term of the energy with the distortion of the unit cell is treated in a perturbative way supposing that the distortion is small with respect to the reference geometry (29).

In order to compute correlations afterwards we projected the obtained relaxed polarization patterns to a basis of basic distortions along x,y and z that can be related with this components of the polarization as Fig. 41 schematizes.

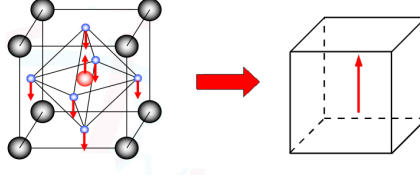


Figure 41: Schematic view of the distortion that forms the basis element for the polarization along the y direction. The modes chosen for x and z directions were the symmetry driven ones of this.

The terms  $E^{(1)}$  and  $E^{(2)}$  are not important in this work since we are always assuming that there are no electronic excitations however they correspond to the full one-electron and two-electron energies respectively produced by the perturbed density (33). In the basis of Wannier functions  $\{|w_a\rangle\}_{a \in orb}$  we can express our bloch functions as

$$|\psi_{i\vec{k}}\rangle = \sum_a c_{ia\vec{k}} e^{i\vec{k}\vec{R}_A} |w_a\rangle, \quad (59)$$

and the electronic density takes the form

$$n(\vec{r}) = \sum_{ab} d_{ab} w_a^*(\vec{r}) w_b(\vec{r}), \quad (60)$$

where  $d_{ab}$  is a matrix that contains the information of the occupation of the orbitals, mathematically

$$d_{ab} = \sum_{i\vec{k}} o_{i\vec{k}} c_{ia\vec{k}}^* c_{ib\vec{k}} e^{i\vec{k}(\vec{R}_A - \vec{R}_B)}. \quad (61)$$

Doing the same approach we did before we can split this density matrix and define the perturbation density matrix as  $d_{ab} = d_{ab}^{(0)} + D_{ab}$  so that

$$\delta n(\vec{r}) = \sum_{ab} D_{ab} w_a^*(\vec{r}) w_b(\vec{r}). \quad (62)$$

With this notation  $E^{(1)}$  and  $E^{(2)}$  take a simple description in terms of  $D_{ab}$

$$E^{(1)} = \sum_{ab} D_{ab} \langle w_a | \hat{h}[n_0] | w_b \rangle, \quad (63)$$

$$E^{(2)} = \sum_{ab} \sum_{a'b'} D_{ab} D_{a'b'} \langle w_a w_{a'} | \frac{1}{|r - r'|} + \frac{\delta^2 E_{xc}}{\delta n(\vec{r}) \delta n(\vec{r}')} \Big|_{n_0} | w_b w_{b'} \rangle, \quad (64)$$

where  $\hat{h}[n_0]$  represents the Hamiltonian associated with the reference density. As we can check, all the parameters of the model are evaluated at the reference state.

Once we have understood the theory underneath the methodology of the calculation I would like to comment some aspects about the Monte Carlo simulations. First of all we run an annealing down to very low temperatures to make the relaxation of the structure and find the ground state of the system at  $T = 0K$ .

Depending on the model in consideration we started the annealing from a monodomain lying along the  $[110]_{pc}$  direction in the case of the first model treated on the main text or from a  $180^\circ$  Ising-like domains along  $[001]_{pc}$  direction in the case of the second model treated on the main text. In the case of the second model multiple minima are found essentially degenerated in energy but differing in the axial component of the polarization  $p_y$ (28) we choose one of the helical structures to continue the work. From that relaxed structures we started to increase the temperature by  $20K$  steps using previous information to compute future structures. Each calculation consisted in 7000 thermalization sweeps followed by 3000 sweeps to compute averages and obtain correlation functions with an overall time of 4 days in the case of the first model or one week in the case of the second model to optimize one structure. Each sweep was conformed by perturbing every cell within the supercell and checking if that change was acceptable or not depending of course in the Boltzmann factor so, in fact, every sweep was formed by  $20 \times 10 \times 20 = 4000$  opportunities to change the state of one unit cell of the supercell.

Due to the size and complexity of the problem together with the constrains on time made not possible to improve the sampling unless for some specific temperatures. These calculations did not pretend to be production ones (which typically are composed by more than 50000 sweeps) but big enough to let us explore the feasibility of this transitions in such systems. However, in future works without time penalties we shall increase the quality of the calculations in order to publish the results.